remote sensing

MDPI

Article

High-Quality Short-Range Radar Imaging with Coprime Sampling

Yaping Wang [1], Tianjiao Zeng [2,*], Xu Zhan [1], Xiangdong Ma [1], Mou Wang [1], Jun Shi [1], Shunjun Wei [1] and Xiaoling Zhang [1]

[1] School of Information and Communication Engineering, University of Electronic Science and Technology of China, Chengdu 611731, China; zhanxu@std.uestc.edu.cn (X.Z.)
[2] School of Aeronautics and Astronautics, University of Electronic Science and Technology of China, Chengdu 611731, China
* Correspondence: tzeng@uestc.edu.cn

Abstract: Short-range imaging radar, with its all-day and all-weather perception capabilities, has gained considerable attention in emerging fields such as autonomous vehicle sensing and industrial robotic perception. However, compared to traditional imaging radar, short-range imaging radar systems face more stringent constraints in terms of physical sampling resources, particularly the number of sampling channels and the resulting aperture size. These limitations lead to reduced resolution and a lower signal-to-noise ratio, ultimately degrading the imaging quality and making it difficult to interpret. To address these challenges, we explore coprime sampling as a strategy to achieve high-quality short-range radar imaging using limited physical sampling resources. Our approach is built upon three core perspectives: (1) physical sampling: we adopt a coprime pattern to form an extended sampling aperture with a structured layout, enabling effective utilization of limited channels and minimizing aperture loss; (2) signal measurement: we utilize the second-order statistics of the measured data to generate additional equivalent measurements, thus enhancing the system's capability to capture diverse spatial information; and (3) scene reconstruction: we establish a novel forward measurement model, linking these equivalent measurements to the scene, and then formulate a sparsity-regularized optimization problem. We design a background-texture-preserving, target-enhanced resolving method based on the first-order proximal gradient algorithm to achieve robust and high-quality imaging results. Our method is verified on several measured data. The results show that our proposed approach achieves high-quality imaging while utilizing approximately half of the typical sampling resources. This study not only validates the effectiveness of coprime sampling for short-range radar imaging but also highlights its potential to alleviate sampling constraints in various resource-constrained applications.

Keywords: short-range imaging radar; coprime sampling; covariance matrix; sparsity-based regularization; resource limited

check for updates

Citation: Wang, Y.; Zeng, T.; Zhan, X.; Ma, X.; Wang, M.; Shi, J.; Wei, S.; Zhang, X. High-Quality Short-Range Radar Imaging with Coprime Sampling. *Remote Sens.* **2024**, *16*, 4657. https://doi.org/10.3390/rs16244657

Academic Editors: Andrzej Stateczny and Stefano Tebaldini

Received: 26 October 2024
Revised: 27 November 2024
Accepted: 11 December 2024
Published: 12 December 2024

Copyright: © 2024 by the authors. Licensee MDPI, Basel, Switzerland. This article is an open access article distributed under the terms and conditions of the Creative Commons Attribution (CC BY) license (https://creativecommons.org/licenses/by/4.0/).

1. Introduction

Short-range imaging radar provides all-day, all-weather perception, making it indispensable compared to other sensing modalities like optical imaging and lidar, which are limited by lighting or atmospheric conditions [1]. It has been used in target scattering imaging for assessing electromagnetic properties [2–8] and in security screening to detect concealed items irrespective of the environment [9–14]. The technology also supports environmental monitoring [15–19] and landslide prediction for public safety [20–22]. Recently, its versatility has expanded to the automotive sector for autonomous vehicle sensing and industrial robotics for precise perception, enabling safe navigation and interaction in complex environments [23–30].

1.1. Problem Formation and Current Status

Compared to traditional imaging radar, short-range imaging radar platforms typically face significant resource constraints. These constraints arise from several factors inherent to short-range radar applications [1,17,31–33]:

- Design Limitations: Short-range radar systems are often designed for compact, portable, or integrated applications, such as autonomous vehicles, drones, mobile robots, and handheld devices . These designs inherently restrict the physical space available for radar components.
- Cost Considerations: These systems are generally aimed at more cost-sensitive markets, limiting the number of expensive components like antenna elements that can be included.
- Power Constraints: Many short-range applications require low power consumption, further constraining the size and complexity of the radar system.
- Integration Challenges: In applications like automotive sensing or drone navigation, the radar must be integrated seamlessly into the vehicle's or device's design, adding another layer of restriction to its size and configuration.

These resource constraints primarily manifest as limitations in the radar's physical aperture and sampling capabilities, creating a cascade of challenges for short-range radar systems:

- Aperture Limitations: Physical size constraints directly impact the aperture—the effective area for transmitting and receiving radar signals. This smaller aperture inherently restricts the antenna size or the number of antenna elements.
- Sampling Constraints: Limited sampling sources—such as a restricted number of antenna elements or sampling points along the aperture—constrain the obtainable aperture size. The Nyquist sampling theorem further compounds this issue by requiring a specific sampling interval, ultimately capping the maximum achievable aperture size.
- Resolution Reduction: Consequently, short-range radar systems often struggle with diminished resolution, making it challenging to differentiate between closely spaced targets.
- Signal-to-Noise Ratio (SNR) Degradation: A smaller aperture collects less signal energy, resulting in a lower signal-to-noise ratio. This is particularly problematic for low-reflectivity targets, which may become indistinguishable from surrounding clutter or noise.

In response to this pressing need, recent research has adapted sparse sampling techniques from traditional imaging radar systems to enhance the capabilities of short-range radar within constrained resources [10–12,14,31,34–39]. Sparse sampling employs highly random, non-uniform sampling patterns to drastically reduce the number of required samples. By leveraging these irregular sampling grids, it becomes possible to reconstruct high-quality images by solving a linear inverse problem, where the sampling pattern itself serves as a critical prior in the system's observation model.

While this approach holds significant promise, particularly for its ability to maintain imaging quality with fewer resources, one crucial factor has yet to be fully addressed: the practical implementation of these designs. The success of sparse sampling hinges on precise control over the pattern layout, which often leads to highly random and unstructured designs that may not be straightforward or cost-effective to produce in practice. Any deviation between the designed and actual patterns can result in a model-mismatch issue during image reconstruction, potentially undermining the very assumptions that guide the reconstruction algorithm. Such deviations can introduce errors and degrade image quality significantly, as the sampling pattern acts as a foundational prior in the observation model [40,41].

1.2. Motivations and Contributions

Given these challenges, it may be necessary to re-evaluate the sampling strategy itself. Traditional uniform sampling offers a structured and deterministic pattern, while sparse sampling represents a fully unstructured approach. A potential way forward lies in finding a balance between these extremes—a sparse yet more structured sampling pattern that can be feasibly and cost-effectively implemented in real-world scenarios while retaining the high-quality imaging performance.

In this context, we explore the concept of coprime sampling—originating from array signal processing for Direction of Arrival (DOA) estimation—and apply it to short-range imaging radar [42–44]. Coprime sampling manifests as the coprime array, consisting of two interleaved subarrays with uniformly distributed elements spaced at coprime intervals larger than the Nyquist sampling theorem requires. For instance, one subarray might have elements spaced at 3 units and the other at 5 units, where 3 and 5 are coprime numbers. This antenna layout results in a sampling pattern we refer to as coprime sampling.

The elegance of this approach lies in its simplicity and effectiveness. By using only two prime numbers, we can define a well-structured sampling pattern that simplifies implementation. Each subarray maintains a uniform distribution, and when combined, they create an overall sparse sampling pattern. This strategy strikes a balance between sparse and uniform sampling, optimizing resource efficiency.

As previously noted, coprime sampling was initially developed for DOA problems, which focus solely on determining target directions. In these applications, targets are typically sparse and characterized by strong, isolated scatterers. Our context, however, differs significantly. We are interested in both target directions and intensities, and our scenes are far more complex. They often involve near-ground environments with abundant vegetation, where targets are typically distributed across the scene—such as vehicles along a road. These complexities mean that traditional DOA-based coprime sampling methods cannot be directly applied or adequately meet the needs of our scenarios. To address these limitations, we have developed several key advancements in high-quality short-range radar imaging using coprime sampling, which, together with the contributions of our work, are outlined below across four core aspects:

1. Physical Sampling: We adopt a coprime pattern to form an extended sampling aperture with a structured layout. This approach enables the effective utilization of limited antenna channels, addressing the resource constraints typical in short-range radar systems.
2. Signal Measurement: We leverage the second-order statistics of the measured data to generate additional equivalent measurements. This approach utilizes the covariance matrix of the physically measured signals, which captures valuable information about the spatial correlations between different measurement points. By exploiting these second-order statistics, we extend beyond the physically measured signals to create equivalent measurements without requiring additional physical sampling resources.
3. Scene Reconstruction: We develop an equivalent forward measurement model that links the new equivalent measurements to the intensity map of the imaging scene. Using this model, we formulate a sparsity-regularized optimization problem for accurate and robust imaging in real-world short-range radar environments. To enhance the interpretation of distributed targets in complex environments, we design a novel background-texture-preserving, target-enhanced resolving method based on the first-order proximal gradient algorithm.
4. Experimental Verification: We evaluate our coprime sampling approach using both simulated and real-world data for short-range radar imaging. Our experiments cover various scenarios, including different target types and environmental conditions. We analyze image quality, comparing our method against traditional uniform sampling and other sparse sampling techniques. This evaluation demonstrates our approach's effectiveness and identifies its strengths in practical applications.

The remainder of this paper is structured as follows. In Section 2, we delve into the fundamental principles of coprime sampling and its application to short-range radar imaging. Then we present our novel approach to signal measurement and scene reconstruction, detailing the mathematical framework and methods we have developed. Section 3 describes our experimental setup and methodology, followed by a thorough presentation and analysis of results. Section 4 shows the discussions about the principles, practical implementations, and comparative advantages of the proposed method. Finally, Section 5 concludes the paper with a summary of our findings, a discussion of the limitations, and suggestions for future research directions in this promising area of radar technology.

2. Materials and Methods

This section begins with the fundamentals of short-range imaging radar with uniform sampling. We review its common types and the common sampling patterns behind them, as well as the key parameters that influence imaging quality.

We then introduce the concept of short-range imaging radar with coprime sampling, discussing its potential limitations when applied to short-range imaging radar. Furthermore, from a signal processing perspective, we design two strategies to achieve high-quality imaging with coprime sampling. First, we explore increasing sampling points from the measurement signal by utilizing its second-order statistical information—the correlations between each sampled signal—to obtain an equivalent measured signal that is more uniform and dense. With this new equivalent signal, we establish a new equivalent forward measurement process from a signal perspective and derive the corresponding equivalent measurement process. Second, to further simplify solving, we establish a new regularization-based solving model, utilizing the sparsity prior of the short-range radar imaging scene. Additionally, considering the importance of background texture for interpreting short-range radar images, a background-texture-preserving, target-enhanced resolving method is designed.

Furthermore, for ease of reading, we summarize this section, the structure of the methodology, in Table 1.

Table 1. Arrangement of the methodology.

Subsection Arrangement	Note
Section 2.1 Short-range Imaging Radar with Uniform Sampling	Baseline Signal Measurement Model
Section 2.2 Short-range Imaging Radar with Coprime Sampling	Proposed Signal Measurement Model
Section 2.3 Equivalent Signal Measurement	Transformation and Preprocessing
Section 2.4 Scene Reconstruction	Imaging and Signal Reconstruction

2.1. Short-Range Imaging Radar with Uniform Sampling

The quality of the imaging result is typically linked to the obtained bandwidth of the imaging scene or target—more specifically, its spatial spectrum [45,46]. The size of the spectrum is proportional to the available resolution after processing. From a mathematical perspective, the spectrum's size is also closely related to the available amount of measurements (the knowns) that can be utilized for resolving the results (the unknowns). Thus, obtaining more of the spectrum boosts the stability of the solution, making it more robust to noise interference.

For short-range radar, the bandwidth in the range direction stems from the transmitted signal bandwidth. Common transmitted types include stepped-frequency pulsed signals or linear-frequency-modulated continuous wave signals [7,30]. The bandwidth from the azimuth direction, which receives more attention and has greater diversity, is physically related to the imaging aperture's size in the azimuth direction—the aperture length or, similarly, the aperture angle.

To achieve higher azimuth signal bandwidth compared to real-aperture single-antenna imaging radar systems, various measurement layout techniques have emerged. Three

types are most prevalent: multichannel-based, motion-synthesis-based, and a hybrid of the two [7,31,46]. We provide a simplified illustration in Figure 1. Figure 1a depicts multichannel-based systems, which use multiple antenna elements arranged in a linear array to form a synthetic aperture. These arrays can be multiple-input-multiple-output (MIMO) or single-input-multiple-output (SIMO), enabling simultaneous data collection across multiple channels. Motion-synthesis-based systems, shown in Figure 1b, rely on the movement of a single antenna to create a synthetic aperture over time. The hybrid approach, illustrated in Figure 1c, combines both methods, using a moving array of multiple antennas to maximize aperture size.

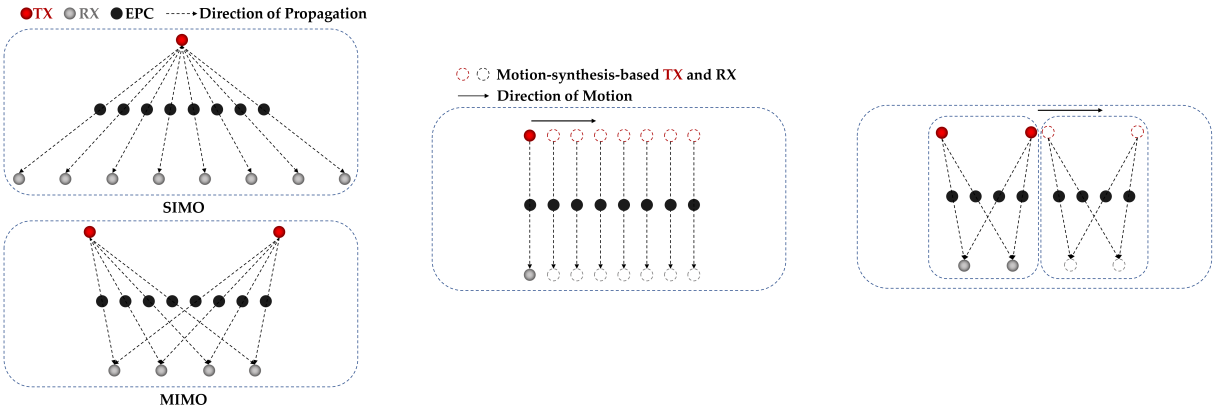


Figure 1. Illustration of three prevalent measurement layout techniques with 8 EPCs. (**a**) Multichannel-based systems: the upper part shows an example of a SIMO array with $N_{TX} = 1$ transmitting antenna and $N_{RX} = 8$ receiving antennas; the lower part depicts an example of a MIMO array with $N_{TX} = 2$ and $N_{RX} = 4$. (**b**) Motion-synthesis-based systems: an example of a single transmitting and receiving antenna's movement to create 8 EPCs. (**c**) A hybrid of the two: an example of a MIMO array's movement with $N_{TX} = 2$ and $N_{RX} = 2$ to create 8 EPCs.

Despite their differences, all these types rely on the principle of the equivalent phase center (EPC). This principle states that a separated multistatic transmitting–receiving antenna pair can be approximated by a colocated monostatic equivalent phase center at the midpoint of the antenna pair, after some preprocessing and compensation [47–50]. Thus, although taking different physical measurement layouts, the final layouts of the EPCs are the same.

From a signal perspective, we can describe a common measurement model for current short-range imaging radar systems. These systems measure the target or imaging scene using uniformly distributed phase centers—sampling points along the azimuth direction—as follows:

$$\mathbf{y}_r = \mathbf{A}_r \mathbf{x}_r + \mathbf{n}_r \tag{1}$$

Here, $\mathbf{y}_r$ represents the measured signal vector at the r-th range unit, typically sized according to the number of sampled points. $\mathbf{A}_r$ is the corresponding measurement matrix, and $\mathbf{x}_r$ denotes the scattering vector of the target or scene. (We follow the Born assumption that the scene or target consists of individual point scatterers without interleaved correlations. The vector's size is determined by the imaging scene's size and the divided pixel size, usually larger than the theoretical resolutions.) $\mathbf{n}_r$ represents noise.

Each column of the measurement matrix encodes the distance information between a target point and each azimuth sampling point as an exponential term. Under certain mild assumptions (This assumption can be understood from multiple perspectives. First, in short-range imaging radar applications, the effective accumulated aperture angle (maximum coherent accumulation) of the target is typically small—only a few degrees. This small angle allows us to neglect the influence of the nonlinear part of the range-induced phase term, as the experimental results demonstrate. In other words, the effective aperture

length is much shorter compared to both the target length and the imaging scene span, thus adhering to the far-field assumption. Secondly, preprocessing techniques can often further support this assumption. It is possible to implement steps that compensate for the nonlinear phase part, resulting in a predominantly linear phase to work with. Additionally, we assume that the measured signal has undergone processing in the range direction, such as range compression, as we mainly focus on the processing in the azimuth direction in this study.), this distance exhibits a linear relationship with the positions of the sampling points. Given the uniform distribution of these sampling points along the azimuth direction, the resulting phase distribution is both linear and uniform [27,31,47]. Consequently, the measurement matrix assumes the form of a Fourier transform matrix, a property that significantly simplifies subsequent analysis and processing.

For different scattering vectors at different range units, the difference between the corresponding measurement matrices can be approximated as a constant range-difference-induced phase term. This term remains constant across different azimuth sampling points and can be ignored as it does not influence the imaging result. Consequently, for the entire imaging scene, the measurement process can be expressed as:

$$\mathbf{Y} = \mathbf{AX} + \mathbf{N} \tag{2}$$

Here, $\mathbf{Y}$ represents the measured signal matrix for the entire imaging scene, with each column corresponding to a specific range unit. $\mathbf{A}$ is the measurement matrix, which remains consistent across all range units due to the aforementioned approximation. $\mathbf{X}$ denotes the scattering matrix of the entire imaging scene, with each column representing the scattering vector at a specific range unit. Finally, $\mathbf{N}$ represents the noise matrix for the entire scene.

Analyzing the measurement equation from a mathematical perspective reveals crucial insights about sampling pattern requirements:

1. Sampling Density: When the scene width is fixed, increasing the number of measurements (i.e., more rows in the measurement matrix) allows for a finer division of the scene (more columns in the scattering matrix). This supports a more detailed reconstruction of the scene.
2. Sampling Uniformity: The uniformity of sampling is equally important. Undersampling or sparse sampling can lead to ill-conditioning of the measurement matrix, making the equation difficult or impossible to solve accurately.

2.2. Short-Range Imaging Radar with Coprime Sampling

As our review indicates, the effectiveness of a sampling strategy in short-range radar imaging hinges on two critical factors: sampling density and uniformity. Sampling density directly influences the level of detail achievable in scene reconstruction, while uniformity ensures the mathematical problem remains well-conditioned and solvable. However, achieving both high density and uniformity is resource-intensive, and short-range imaging radar systems often face limitations in this regard.

Given these constraints, striking a balance between sampling density and uniformity is crucial for obtaining high-quality imaging results. To address this challenge, we introduce a novel coprime sampling strategy in this subsection. Coprime sampling primarily refers to the sampling distance between adjacent points being coprime. We present an illustration of this concept in Figure 2. In this example, there are a total of seven sampling points available, spanning a length of 12 units. From left to right, the distance between the first, second, fourth, fifth, and last point is 3 units, while the distance between the first, third, and sixth point is 5 units. Mathematically, 3 and 5 are a pair of coprime numbers.

From this example, we can see that the most distinct feature and advantage is the convenience of determining the sampling pattern. By defining a pair of coprime numbers, we can immediately obtain a structured sampling pattern. Mathematically, if we denote

the unit length as d and a pair of coprime numbers as M and $N(M < N)$, we can generate two sub-sampling patterns. By fusing these, we obtain the overall sampling pattern.

- Sub-sampling pattern 1:

$$\{0, Md, 2Md, \cdots, (N-1)Md\}$$

- Sub-sampling pattern 2:

$$\{0, Nd, 2Nd, \cdots, (M-1)Nd\}$$

- Overall sampling pattern:

$$\{0, Md, 2Md, \cdots, (N-1)Md\} \cup \{0, Nd, 2Nd, \cdots, (M-1)Nd\}$$

Through this sampling method, we use $(M + N - 1)$ sampling points to achieve a sampling length of $M(N-1)$ units. Compared to uniform sampling, the advantage extends beyond the structured pattern to resource efficiency. If we have only $M + N$ sampling points available, we gain an extra sampling length ratio of $(M(N-1)/(M+N-1)-1)$ units. Conversely, if we need a sampling length of MN units, we can reduce the required sampling points by a factor of $(M + N - 1)/(M(N-1)+1)$. Taking the example in Figure 2, we halve the resource cost while achieving a similar sampling length.

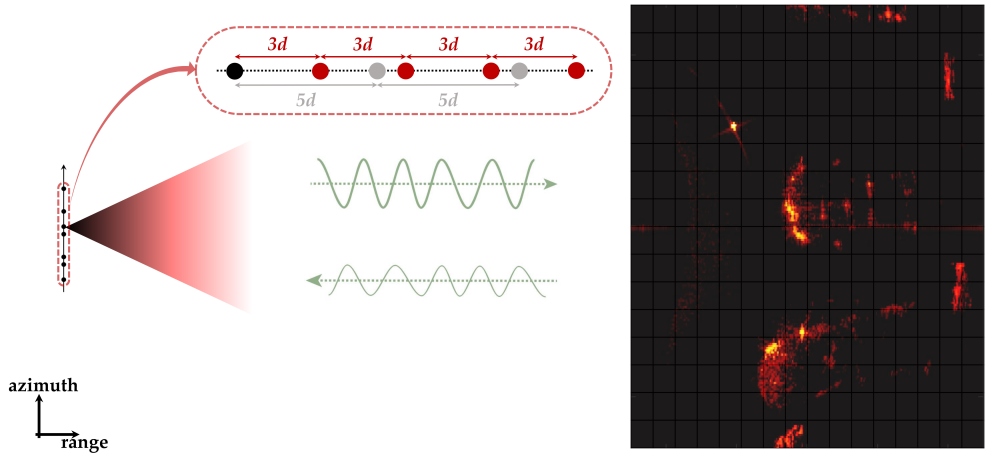


Figure 2. Illustration of coprime sampling measurement layout with 7 antennas.

Similar to equation (1), we can express the corresponding measurement process as:

$$\mathbf{Y_c} = \mathbf{A_c X} + \mathbf{N} \tag{3}$$

Here, $\mathbf{Y_c}$ represents the new measured signal matrix with coprime sampling, and $\mathbf{A_c}$ is the new measurement matrix. $\mathbf{A_c}$ can be viewed as a subset of the uniform sampling measurement matrix $\mathbf{A}$, obtained by removing the rows corresponding to unsampled points.

Due to this subtraction, the ill-posedness of the new measurement equation increases significantly. Short-range radar typically operates in an environment with stronger noise and clutter from surroundings compared to conventional airborne or spaceborne situations, as the system is much closer to the ground [31]. Consequently, solving the new equation using traditional methods, especially matched-filtering-based algorithms [51,52], would be highly inaccurate and unstable. More specifically, as the measurement matrix takes the form of the inverse Fourier transform, each sub-sampling measurement introduces azimuth ambiguities—the grating lobes of targets. Although each sub-sampling pattern has different sub-sampling scenarios, resulting in azimuth ambiguities at different positions, merging the results using these differences in ambiguity locations can reduce the total ambiguities to a certain degree [53,54]. However, this approach imposes additional requirements on the

target's distribution and size in the imaging scene, necessitating much sparser scenes, such as maritime environments (ships at sea) [53,54]. In short, the direct introduction of coprime sampling for short-range radar may not yield sufficient performance gains. Therefore, we propose further processing from a signal processing perspective, beyond this modification of physical measurement patterns.

2.3. Equivalent Signal Measurement

In the previous section, we introduced the new physical layout of coprime sampling for short-range imaging radar and established the new forward measurement process and equation in (3). Analysis of this new measurement equation reveals challenges in solving it, necessitating further processing from a signal processing perspective. To achieve high-quality imaging with coprime sampling, this section explores the generation of equivalent measurements using the covariance matrix of physically measured signals obtained by coprime sampling.

2.3.1. Basic Ideas

In this section, we examine the correlations between every pair of physical measurement points to identify additional equivalent measurement points. Recall the measurement process and equation in (3); it is evident that some measurement points from the uniform measurement equation in (1) are missing. For simplicity, we will continue with the example using coprime numbers 3 and 5. As illustrated in Figure 2, measurement points at locations $1d$, $2d$, $4d$, $7d$, $8d$, and $11d$ are missing compared to the uniform sampling case. Conversely, measurement points at locations $0d$, $3d$, $5d$, $6d$, $9d$, $10d$, and $12d$ are available. For these physically measured points, let us consider the measured signal at location $0d$ as an example. Based on (3), it can be expressed as follows.

$$y_0 = \sum_{p=0}^{P} x_p e^{j0p\Delta\phi} + n_0 \tag{4}$$

Here, we take one range unit profile within the scene as an example. We use the symbol l to index the locations of measured points, which range from 0 to L, with $L = 12$ in this example. We use the symbol p to index the locations of the scatterers within the corresponding range unit. We divide the range unit into a grid of $P + 1$ points, with p ranging from 0 to P. n_0 represents the independent complex Gaussian noise, which has a zero mean and variance ε_n^2. x_p denotes the complex scattering coefficient. The term $e^{j0p\Delta\phi}$ represents the range-induced phase, which varies linearly with the scatterer's index p.

Similarly, for the point at location $1d$, if we could obtain its measurement, it would be expressed as follows.

$$y_1 = \sum_{p=0}^{P} x_p e^{j1p\Delta\phi} + n_1 \tag{5}$$

With some modifications, we can express the statistically equivalent form as follows.

$$\begin{aligned} \mathbb{E}[y_6 y_5^*] &= \mathbb{E}\left[\left(\sum_{p=0}^{P} x_p e^{j6p\Delta\phi} + n_6\right)\left(\sum_{p=0}^{P} x_p^* e^{-j5p\Delta\phi} + n_5^*\right)\right] \\ &= \sum_{p=0}^{P} |x_p|^2 e^{j1p\Delta\phi} \end{aligned} \tag{6}$$

Here, $\mathbb{E}[\cdot]$ denotes the expectation operation. Comparing the above two equations, we can see that through the correlation and expectation of the physically measured signals at locations $6d$ and $5d$, we can obtain a statistically equivalent form of the measured signal at location $1d$ from a signal processing perspective. The resulting equivalent signal shares the

same form as the physical measured signal, except it measures the power distribution of the scatterers within the scene instead of the complex intensity distribution.

This observation inspires us to use second-order statistical information from physically measured signals to obtain equivalent signals with denser, more uniform sampling points. We turn to the covariance matrix, which contains all pairwise correlation information from the measured signals. Specifically, we compute the covariance matrix of the measured signal $\mathbf{y_c}$ for each range unit as follows.

$$\mathbf{R} = \mathbb{E}\left(\mathbf{y_c}\mathbf{y_c}^{\mathrm{H}}\right) = \sum_{p=0}^{P} |x_p|^2 \mathbf{a}(\phi_p)\mathbf{a}^{\mathrm{H}}(\phi_p) + \varepsilon_n^2 \mathbf{I} \tag{7}$$

Here, $(\cdot)^H$ denotes the Hermitian transpose, and $\mathbf{a}(\phi_p) = [e^{j0p\Delta\phi}, e^{j1p\Delta\phi}, \ldots, e^{jLp\Delta\phi}]^T$ is the range-induced phase at different sampled locations of the p-th scatterer. Notably, in coprime sampling, some of the range-induced phases are unavailable. For simplicity, we insert zeros for these missing values in the measured signal and the range-induced phase. Using our previous example,

$$\mathbf{a}(\phi_p) = [e^{j0p\Delta\phi}, 0, 0, e^{j3p\Delta\phi}, 0, e^{j5p\Delta\phi}, e^{j6p\Delta\phi}, 0, 0, e^{j9p\Delta\phi}, e^{j10p\Delta\phi}, 0, e^{j12p\Delta\phi}]^T \tag{8}$$

And the element in the covariance matrix takes the following form:

$$r_{m,n} = \begin{cases} \sum_{p=0}^{P} |x_p|^2 e^{j(m-n)p\Delta\phi}; m \neq n \\ \sum_{p=0}^{P} |x_p|^2 e^{j(m-n)p\Delta\phi} + \varepsilon_n^2; m = n \end{cases} \tag{9}$$

We further denote $r_{m,n}$ as $\tilde{y}_{m-n}$, $|x_p|^2$ as $\tilde{x}_p$, $(m-n)$ as l, and noise as $\tilde{n}$, obtaining the equivalent measurement $\tilde{y}_l$ in general:

$$\tilde{y}_l = \sum_{p=0}^{P} \tilde{x}_p e^{jlp\Delta\phi} + \tilde{n} \tag{10}$$

Equation (10) indicates that $\tilde{y}_l$ can be considered as the equivalent measurement at the $l = (m-n)$-th sampling point. For instance, when $m = 3$, and $n = 1$, then $l = 2$, $\tilde{y}_2$ is the equivalent measurement at the 2nd sampling point. All equivalent measurements, embedded in the covariance matrix, can be defined through the difference operation of various pairs $(m-n)$.

Figure 3 provides a visual example. There are 7 sampling points with the position set denoted as $\mathbf{S} = \{0, 3, 5, 6, 9, 10, 12\}$ shown in the upper part of Figure 3. By taking the difference operations from paired elements of $\mathbf{S}$, we obtain a new set $\mathbf{D} = \{0, 1, 2, 3, 4, 5, 6, 7, 9, 10, 12\}$, which contains 11 elements corresponding to 11 sampling points shown in the lower part of Figure 3. Compared to the physical sampling, there are 4 additional sampling points, making the whole sampling pattern denser and more uniform. The extra sampling points are represented by dashed lines in Figure 3.

2.3.2. Technical Details

Based on these ideas, we now delve into the technical details of generating equivalent signal measurements. In theory, we need to determine the mean value of the correlations between measurement pairs in Equation (7), which would require an infinite number of samples. In practice, however, we are limited to a finite sample set. To mitigate estimation errors, we intuitively seek to increase our sample size for estimation. We achieve this through two methods: first, by exploiting the redundancy in adjacent range unit samples

for covariance matrix estimation; and second, by utilizing the redundancy in diagonal elements within the covariance matrix for equivalent measured signal estimation.

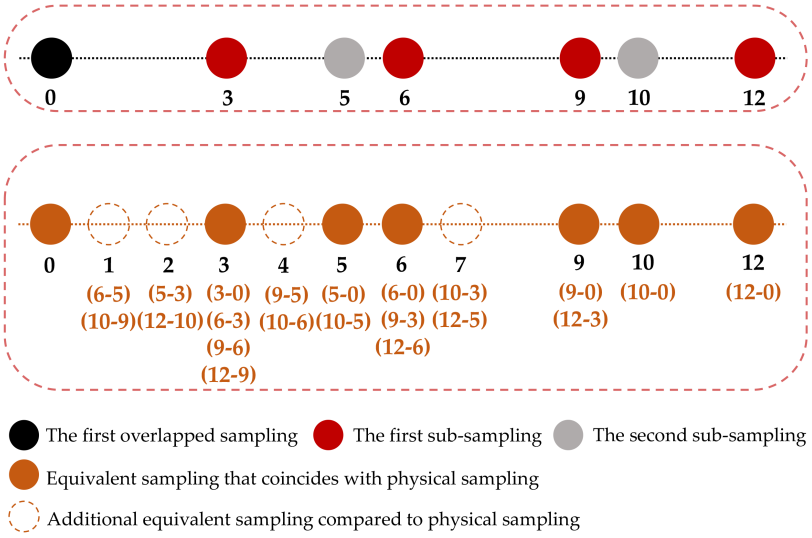


Figure 3. Diagram of equivalent measurements utilizing second-order statistics. The upper part shows coprime samples with 7 EPCs and the lower part depicts equivalent samples with 11 EPCs.

1. Redundancy in adjacent range unit samples.

Considering that targets are usually extended and distributed across several adjacent range units, they typically follow the same statistical distribution. Specifically, the adjacent scatterers within each target have similar spatial locations, and their intensities remain fixed and non-fluctuating [55]. We adopt multiple adjacent range units to estimate the covariance matrix. For each range unit, we employ a sliding window with length $T+1$ centered on the current unit to acquire its adjacent units. We then use the mean of covariance matrices corresponding to these units to estimate the covariance matrix $\hat{\mathbf{R}}$. For example, for the r-th range unit,

$$\hat{\mathbf{R}}(r) = \frac{1}{T+1} \sum_{t=r-T/2}^{t=r+T/2} \mathbf{Y_c}(t) \mathbf{Y_c}^{\mathrm{H}}(t) \tag{11}$$

Here, $\mathbf{Y_c}(t)$ represents the t-th range unit's zero-inserted measured signal.

2. Redundancy in diagonal elements within the covariance matrix.

Considering that the target signal is usually stationary, the diagonal elements within the covariance matrix can be considered as samples from the same distribution. In other words, $\tilde{r}_{m,n} = \tilde{r}_{m+1,n+1}$. Using our previous example, we can obtain the covariance matrix as follows:

$$\hat{\mathbf{R}}(r) = \begin{bmatrix}
\tilde{r}_{0,0} & 0 & 0 & \tilde{r}^*_{3,0} & 0 & \tilde{r}^*_{5,0} & \tilde{r}^*_{6,0} & 0 & 0 & \tilde{r}^*_{9,0} & \tilde{r}^*_{10,0} & 0 & \tilde{r}^*_{12,0} \\
0 & 0 & 0 & 0 & 0 & 0 & 0 & 0 & 0 & 0 & 0 & 0 & 0 \\
0 & 0 & 0 & 0 & 0 & 0 & 0 & 0 & 0 & 0 & 0 & 0 & 0 \\
\tilde{r}_{3,0} & 0 & 0 & \tilde{r}_{3,3} & 0 & \tilde{r}^*_{5,3} & \tilde{r}^*_{6,3} & 0 & 0 & \tilde{r}^*_{9,3} & \tilde{r}^*_{10,3} & 0 & \tilde{r}^*_{12,3} \\
0 & 0 & 0 & 0 & 0 & 0 & 0 & 0 & 0 & 0 & 0 & 0 & 0 \\
\tilde{r}_{5,0} & 0 & 0 & \tilde{r}_{5,3} & 0 & \tilde{r}_{5,5} & \tilde{r}^*_{6,5} & 0 & 0 & \tilde{r}^*_{9,5} & \tilde{r}^*_{10,5} & 0 & \tilde{r}^*_{12,5} \\
\tilde{r}_{6,0} & 0 & 0 & \tilde{r}_{6,3} & 0 & \tilde{r}_{6,5} & \tilde{r}_{6,6} & 0 & 0 & \tilde{r}^*_{9,6} & \tilde{r}^*_{10,6} & 0 & \tilde{r}^*_{12,6} \\
0 & 0 & 0 & 0 & 0 & 0 & 0 & 0 & 0 & 0 & 0 & 0 & 0 \\
0 & 0 & 0 & 0 & 0 & 0 & 0 & 0 & 0 & 0 & 0 & 0 & 0 \\
\tilde{r}_{9,0} & 0 & 0 & \tilde{r}_{9,3} & 0 & \tilde{r}_{9,5} & \tilde{r}_{9,6} & 0 & 0 & \tilde{r}_{9,9} & \tilde{r}^*_{10,9} & 0 & \tilde{r}^*_{12,9} \\
\tilde{r}_{10,0} & 0 & 0 & \tilde{r}_{10,3} & 0 & \tilde{r}_{10,5} & \tilde{r}_{10,6} & 0 & 0 & \tilde{r}_{10,9} & \tilde{r}_{10,10} & 0 & \tilde{r}^*_{12,10} \\
0 & 0 & 0 & 0 & 0 & 0 & 0 & 0 & 0 & 0 & 0 & 0 & 0 \\
\tilde{r}_{12,0} & 0 & 0 & \tilde{r}_{12,3} & 0 & \tilde{r}_{12,5} & \tilde{r}_{12,6} & 0 & 0 & \tilde{r}_{12,9} & \tilde{r}_{12,10} & 0 & \tilde{r}_{12,12}
\end{bmatrix} \tag{12}$$

Aligning with the illustration in Figure 3, the equivalent measured signal at location $1d$ can be estimated by averaging $\tilde{r}_{6,5}$ and $\tilde{r}_{10,9}$. Similarly, the equivalent measured signal at location $3d$ can be estimated by averaging $\tilde{r}_{3,0}$, $\tilde{r}_{6,3}$, $\tilde{r}_{9,6}$, and $\tilde{r}_{12,0}$. Other locations follow a similar rule, as shown below:

$$\tilde{y}_l = \text{mean}\left(\text{diag}\left(\hat{\mathbf{R}}(r;l)\right)\right) \tag{13}$$

Here, $\tilde{y}_l$ is the equivalent measurement of the l-th sampling point, $\text{diag}\left(\hat{\mathbf{R}}(r;l)\right)$ denotes the l-th diagonal vector with zeros excluded, and $\text{mean}(\cdot)$ represents the averaging operation.

By averaging the non-zero elements of each diagonal in the zero-filled covariance matrix, we can obtain the final equivalent measured signal $\tilde{\mathbf{y}}_\mathbf{c}$ as follows:

$$\tilde{\mathbf{y}}_\mathbf{c} = [\tilde{y}_0, \tilde{y}_1, \tilde{y}_2, \tilde{y}_3, \tilde{y}_4, \tilde{y}_5, \tilde{y}_6, \tilde{y}_7, \tilde{y}_9, \tilde{y}_{10}, \tilde{y}_{12}]^{\mathrm{T}} \tag{14}$$

Here, $\tilde{\mathbf{y}}_\mathbf{c}$ represents the equivalent measured signal. Finally, we present the complete generation process in Figure 4. Specifically, sets of measured signals within adjacent range units are first used to construct the covariance matrix. Then, the covariance matrix is inserted with zeros, and the elements along each diagonal line are utilized to obtain the equivalent measured signal.

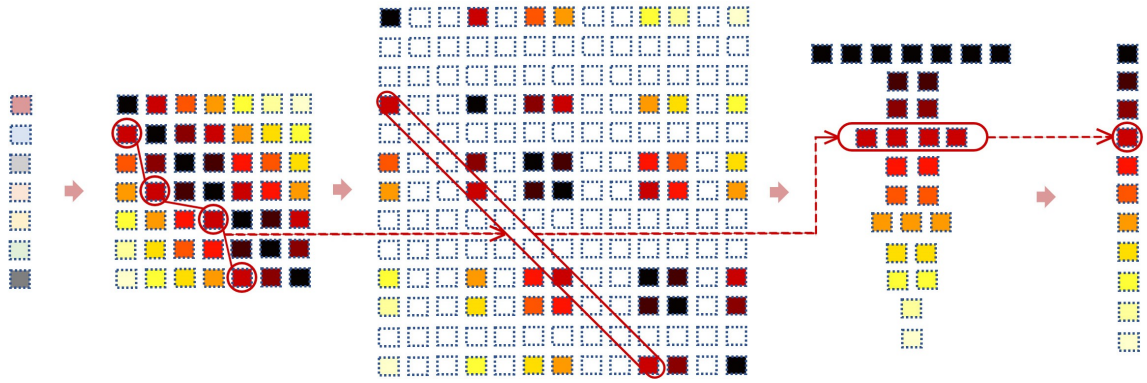


Figure 4. Generation process of equivalent measurements.

2.4. Scene Reconstruction

In this section, we establish an equivalent forward measurement model for these measurements and construct the corresponding sparsity-regularized optimization problem. Simultaneously, we introduce a novel background-texture-preserving, target-enhanced resolving method based on the first-order proximal gradient algorithm.

1. Equivalent Forward Measurement Model

Combining (14) and (10), we can derive the following new equivalent measurement process and equation for the r-th range unit:

$$\tilde{\mathbf{y}}_\mathbf{c} = \tilde{\mathbf{A}}_\mathbf{c}\tilde{\mathbf{x}} + \tilde{\mathbf{n}} \tag{15}$$

Here, $\tilde{\mathbf{y}}_\mathbf{c}$ is the equivalent measured signal, $\tilde{\mathbf{A}}_\mathbf{c}$ is the new forward measurement matrix with $\tilde{\mathbf{A}}_\mathbf{c}(l,p) = e^{jlp\Delta\phi}$, $\tilde{\mathbf{x}}(p) = \tilde{x}_p$ represents the power distribution of the scatterers within the scene, and $\tilde{\mathbf{n}}$ denotes the noise.

Examining Equation (14), we find that the new equivalent measured signal, while offering more available samples through the utilization of physical signal correlations compared to the original signal in (3), still has gaps at certain positions. For instance, the

signal is missing at locations $8d$ and $11d$. This absence can be viewed as an extraction process, allowing us to formulate the above process as follows.

$$\tilde{\mathbf{y}}_{\mathbf{c}} = \mathbf{M}_{\mathbf{c}}\mathbf{A}\tilde{\mathbf{x}} + \tilde{\mathbf{n}} \tag{16}$$

Here, $\mathbf{M}_{\mathbf{c}}$ denotes the extraction matrix, which is derived by removing specific rows from an identity matrix. For the example in (14), it would be the matrix obtained by subtracting the 9th and 12th rows from a 13-by-13 identity matrix.

Recall that the forward measurement matrix $\mathbf{A}$ takes the form of an inverse discrete Fourier transform. This means we can replace it with the inverse fast Fourier transform operator to achieve a more efficient form, as follows:

$$\tilde{\mathbf{y}}_{\mathbf{c}} = \mathbf{M}_{\mathbf{c}}\mathcal{F}^{-\mathbf{1}}(\tilde{\mathbf{x}}) + \tilde{\mathbf{n}} \tag{17}$$

Here, $\mathcal{F}^{-1}(\cdot)$ denotes the operator of the inverse fast Fourier transform.

For the entire imaging scene, we concatenate equations from different range units to obtain the complete equivalent forward measurement process and equation:

$$\tilde{\mathbf{Y}}_{\mathbf{c}} = \mathbf{M}_{\mathbf{c}}\mathcal{F}^{-\mathbf{1}}\left(\tilde{\mathbf{X}}\right) + \tilde{\mathbf{N}} \tag{18}$$

Here, the $\mathcal{F}^{-1}(\cdot)$ operator acts along the azimuth dimension.

2. Sparsity-Regularized Solution

To obtain the imaging result, we need to solve the new equivalent measurement equation, which presents a typical inverse problem scenario. We aim to derive the energy distribution of the scene $\tilde{\mathbf{X}}$ from the equivalent measured signal $\tilde{\mathbf{Y}}_{\mathbf{c}}$.

Following the traditional matched-filtering approach, we mathematically establish a regularization between the equivalent measured signal and the scene. This takes the form of $\|\tilde{\mathbf{Y}}_{\mathbf{c}} - \mathbf{M}_{\mathbf{c}}\mathcal{F}^{-1}\left(\tilde{\mathbf{X}}\right)\|_F^2$, which ensures the solution adheres to the forward measurement model.

Additionally, the short-range imaging radar's working environment deserves attention. The system's proximity to the ground creates a complex surrounding environment. The clutter and noise are relatively high compared to the measured signal, making the solution process susceptible to interference. Consequently, it is crucial to introduce additional regularization constraints. These constraints, such as prior regularizations, describe assumptions about the characteristics of the results (the unknowns), thereby producing reconstructions that align more closely with their original prior distribution.

Considering the short-range imaging radar's scene, a common assumption is that the target within the scene consists of a few strong scatterers and abundant background texture. In other words, the scene exhibits sparsity in the spatial domain—a feature that can be regularized and measured using the l_1 norm. Consequently, we add a sparsity regularization term to obtain the complete optimization problem for solving the equation.

$$\hat{\mathbf{X}} = \arg\min_{\tilde{\mathbf{x}}} \frac{1}{2}\|\tilde{\mathbf{Y}}_{\mathbf{c}} - \mathbf{M}_{\mathbf{c}}\mathcal{F}^{-1}\left(\tilde{\mathbf{X}}\right)\|_F^2 + \lambda\left\|\tilde{\mathbf{X}}\right\|_1 \tag{19}$$

Here, $\hat{\mathbf{X}}$ represents the imaging result, $\|\cdot\|$ denotes the matrix Frobenius Norm, and λ is the weight that balances the two regularization terms.

The above optimization problem can be efficiently solved via first-order proximal algorithms [56,57], where generally the first regularization term is dealt with through gradient descent and the second regularization term is dealt with through proximal mapping in a fixed-point iterative manner as follows [56,57].

$$\tilde{\mathbf{X}}^{k+1} = \mathcal{S}_{\rho\lambda}\left(\tilde{\mathbf{X}}^k + \rho{\mathbf{M}_{\mathbf{c}}}^H\mathcal{F}\left(\tilde{\mathbf{Y}}_{\mathbf{c}} - \mathbf{M}_{\mathbf{c}}\mathcal{F}^{-1}\left(\tilde{\mathbf{X}}^k\right)\right)\right) \tag{20}$$

Here, ρ denotes the step size for gradient descent, and $\mathcal{S}_{\rho\lambda}(\cdot)$ represents the soft-thresholding operator.

In the context of short-range imaging radar, we design an iterative solution process based on the steps above. This process aims to reconstruct the target within the scene, which consists of a few strong scatterers and abundant background texture, while avoiding interference from noise and other disturbances.

Step 1. Update the part of the strong scatterers, filtering out interferences.

$$\tilde{\mathbf{X}}_{\mathbf{s}}^{k+1} = \text{sign}\left(\tilde{\mathbf{X}}^{k}\right) \odot \max\left(\left|\tilde{\mathbf{X}}^{k}\right| - \rho\lambda\mathbf{I}, \mathbf{0}\right) \tag{21}$$

Here, $\text{sign}(\cdot)$ denotes the sign function, which returns the sign of each element. $\odot$ represents the Hadamard product, which is the element-wise multiplication between two matrices. Lastly, $\max(\cdot)$ refers to the clipping function, which sets any negative values to zero. All functions are applied element-wise to the matrices.

In this step, the entire reconstruction result $\tilde{\mathbf{X}}^{k}$ from the last iteration is filtered to extract the strong scatterers, while the residual interferences are removed.

Step 2. Update the part of the background texture.

$$\tilde{\mathbf{X}}_{\mathbf{b}}^{k+1} = {\mathbf{M}_{\mathbf{c}}}^{H}\mathcal{F}\left(\tilde{\mathbf{Y}}_{\mathbf{c}} - \mathbf{M}_{\mathbf{c}}\mathcal{F}^{-1}\left(\tilde{\mathbf{X}}_{\mathbf{s}}^{k+1}\right)\right) \tag{22}$$

In this step, the newly updated strong scatterers undergo a forward measurement process, generating a pseudo-measured signal. This signal is then subtracted from the original measured signal, leaving a residual signal related to the background texture. The remaining signal is processed through the adjoint operations of the forward measurement process—$\mathcal{F}(\cdot)$ and ${\mathbf{M}_{\mathbf{c}}}^{H}$—to reconstruct the background texture component.

Step 3. Update the entire reconstruction result.

$$\tilde{\mathbf{X}}^{(k+1)} = \tilde{\mathbf{X}}_{\mathbf{s}}^{k+1} + \rho\tilde{\mathbf{X}}_{\mathbf{b}}^{k+1} \tag{23}$$

In this step, the overall reconstruction result is updated by combining the strong scatterers component and the weighted background texture component. By merging these two parts, the reconstructed target image becomes more interpretable for subsequent higher-level tasks of short-range imaging radar, such as target detection and classification [58,59].

Step 4. Perform residual update.

$$Resi = \left\|\tilde{\mathbf{X}}^{(k+1)} - \tilde{\mathbf{X}}^{(k)}\right\|_{F} \tag{24}$$

When the *Resi* falls below a specified small constant ε or the number of iterations reaches the upper limit $k_{\max}$, the entire iteration process is terminated.

This iterative process progressively refines the reconstruction by separating and updating the strong scatterers and background texture, enhancing robustness against noise. The final reconstruction is detailed and noise-resistant, making it well-suited for downstream applications such as detection and identification in short-range imaging radar systems. Finally, we summarize the specific implementation steps for scene reconstruction in Algorithm 1.

In summary, for the short-range imaging radar system under the coprime sampling pattern, the proposed high-quality imaging method mainly consists of two parts: equivalent signal measurement and scene reconstruction which are detailed in Sections 2.3 and 2.4. The flowchart of the proposed processing method is shown in Figure 5.

Algorithm 1 Scene Reconstruction Method

Input: $\tilde{\mathbf{Y}}_\mathbf{c}, \tilde{\mathbf{X}}^{(1)} = \mathbf{M_c}^H \mathcal{F}(\tilde{\mathbf{Y}}_\mathbf{c}), \tilde{\mathbf{X}}_s^{(1)} = \mathbf{0}, \tilde{\mathbf{X}}_b^{(1)} = \mathbf{0}, k = 1, k_{\max}, \text{Resi} = 0, \lambda > 0, \rho > 0, \varepsilon > 0$
repeat
  Step 1: Update the part of the strong scatterers
  $\tilde{\mathbf{X}}_\mathbf{s}^{k+1} = \text{sign}\left(\tilde{\mathbf{X}}^k\right) \odot \max\left(\left|\tilde{\mathbf{X}}^k\right| - \rho\lambda\mathbf{I}, \mathbf{0}\right)$
  Step 2: Update the part of the background texture
  $\tilde{\mathbf{X}}_\mathbf{b}^{k+1} = \mathbf{M_c}^H \mathcal{F}\left(\tilde{\mathbf{Y}}_\mathbf{c} - \mathbf{M_c}\mathcal{F}^{-1}\left(\tilde{\mathbf{X}}_\mathbf{s}^{k+1}\right)\right)$
  Step 3: Update the entire reconstruction result
  $\tilde{\mathbf{X}}^{k+1} = \tilde{\mathbf{X}}_\mathbf{s}^{k+1} + \rho\tilde{\mathbf{X}}_\mathbf{b}^{k+1}$
  Step 4: Perform residual update
  $\text{Resi} = \left\|\tilde{\mathbf{X}}^{k+1} - \tilde{\mathbf{X}}^k\right\|_F$
  $k = k + 1$
until $k = k_{\max}$ or $\text{Resi} < \varepsilon$
Output: $\tilde{\mathbf{X}}^{k+1}$

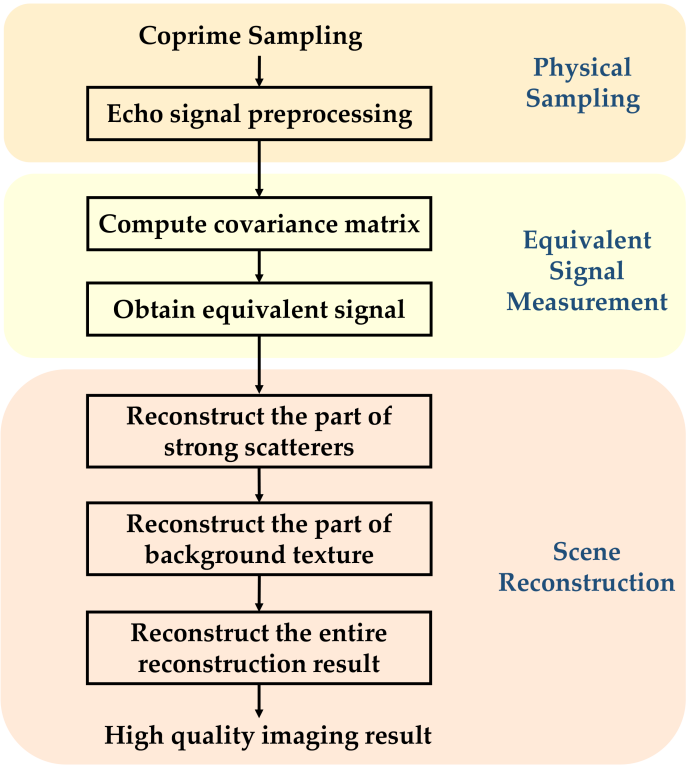


Figure 5. Flowchart of the proposed processing method.

3. Results

In this section, we evaluate the potential for high-quality imaging in short-range radar systems using coprime sampling. We conduct both comparative experiments and ablation studies on the proposed method. In the comparative experiments, the proposed method is compared with traditional uniform sampling and sparse sampling methods. In the ablation studies, we investigate the key components of the proposed method, including equivalent signal measurement and sparse reconstruction, to verify their effectiveness and importance. In the experiments, to quantitatively evaluate the quality of the imaging results, particularly in terms of robustness against noise, accuracy, and preservation of texture information,

we adopt three metrics for evaluation: Peak Signal-to-Noise Ratio (PSNR) [60], Structural Similarity Index (SSIM) [61], and Gradient Magnitude Similarity (GMS) [62].

3.1. Comparative Experiments

In this section, we compare the proposed method with other traditional sampling methods to demonstrate its superiority. We begin by briefly introducing the test scenes and comparative methods.

3.1.1. Test Scenes

We evaluate using a strategy of gradually increasing complexity. The imaging scenes contain targets ranging from simple to complex, and from manually controlled to practical scenarios. In total, we include four test scenes: one simulated and three measured from two different real systems. These scenarios are briefly introduced as follows.

1. Test Scene 1: Uniform Energy Point Array
   This scenario simulates an ideal point target array where all targets have uniform energy levels. It is designed to evaluate the algorithm's basic performance and resolution capabilities.
2. Test Scene 2: Point Array with Varying Energy Levels
   This scenario involves an evenly distributed point array with a wide dynamic range of energy levels. It tests the algorithm's ability to handle targets of varying intensities.
3. Test Scene 3: Controlled Layout with Complex Targets
   This scenario features a manually controlled layout of complex, distributed targets, including objects of different shapes and sizes. It aims to evaluate the algorithm's performance under more realistic and challenging conditions.
4. Test Scene 4: Real-World Parking Lot Scenario
   This scenario involves a real-world layout, such as a parking lot, with various vehicles and ground features. It is used to assess the algorithm's performance in practical, application-oriented situations.

3.1.2. Test Methods

We adopt a total of three methods through the above four test scenes as follows. The three methods compare different sampling patterns and their corresponding imaging algorithms to verify that the proposed algorithm can achieve high-quality imaging results under the coprime sampling.

1. Method 1: Range Migration Algorithm with Uniform Sampling (RMA_Uniform)
   This method uses the range migration algorithm under uniform sampling conditions, which ensures computational efficiency but is constrained by the requirement for uniform sampling [9,23,27].
2. Method 2: Sparsity-Based Regularization Method with Sparse Sampling (l_1_Sparse)
   This method is implemented under a sparse sampling pattern with a sparsity-based regularization approach which has gained recent research interest [11,31]. Different from uniform sampling and coprime sampling, random sparse sampling is a highly random and non-uniform sampling pattern design, which makes it difficult to implement in practice.
3. Method 3: Proposed Method
   The proposed method operates in the equivalent domain of the measured signal, focusing on both strong point scatterers and background textures to achieve a more comprehensive reconstruction.

3.1.3. Experiment Result of Test 1 (Uniform Energy Point Array)

In this section, we simulate 3×3 point array targets with uniform energy to verify the effectiveness of the proposed method. These 3×3 point array targets are arranged in a 10 m $\times$ 10 m grid and uniformly distributed, with their center 15 m away from the radar, as shown in the Figure 6. In this experiment, the radar aperture is synthesized by the repeated

moving, three times, of the coprime sampling depicted in Figure 2, with the synthesized aperture length of $36d$, i.e., 0.0684 m. The radar signal carrier frequency is 78 GHz with around 0.4 GHz bandwidth. The radar parameters are listed in Table 2.

Table 2. Radar parameters.

Parameters	Values
Carrier frequency	78 GHz
Bandwidth	0.4 GHz
Aperture length	0.0684 m
Physical sampling points	19
Equivalent sampling points	35

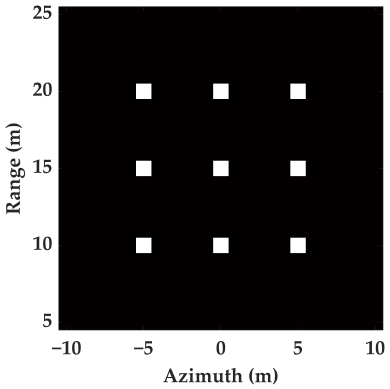


Figure 6. Test 1: 3 × 3 point array targets.

1. Experiment Result Analysis

In the simulation, we utilize coprime sampling with seven equivalent phase centers to synthesize an aperture of $36d$ in length by moving the radar in the azimuth direction. The number of sampling points in the azimuth direction is 19, which can reduce the antenna resources by nearly half compared to uniform sampling with the same aperture size. Moreover, the 19 physical sampling points can generate 35 equivalent sampling points to obtain more equivalent measurements, and the increase in measurements can more effectively enhance the imaging's robustness against noise. We conducted simulations with the SNR at −10 dB, 0 dB, 10 dB, and 20 dB.

Figure 7 presents the results. The first column (Figure 7(a)-1,(b)-1,(c)-1,(d)-1) shows that the RMA_Uniform method achieves relatively complete imaging results for the 3 × 3 point array targets. However, these results exhibit high sidelobe interference, strong background clutter, and poor robustness to noise.

The second column (Figure 7(a)-2,(b)-2,(c)-2,(d)-2) displays the imaging results of the l_1_Sparse method. These results effectively suppress severe grating lobe interference and background clutter, demonstrating that directly applying the l_1_Sparse method can achieve high-quality imaging results. However, as this approach focuses solely on the strong scattering points within the target, it results in some isolated discrete points in the output, which ultimately diminishes the overall imaging quality.

The last column (Figure 7(a)-3,(b)-3,(c)-3,(d)-3) shows the imaging results of the proposed method. The results are comparable to those obtained using sparse sampling methods, with the added benefit of eliminating isolated discrete scattering points. Specifically, background clutter is reduced, and grating lobe interference is suppressed, resulting in a noticeable improvement in imaging accuracy and structure preservation. Even in the low SNR scenario of −10 dB, most scatterers are well reconstructed, demonstrating the effectiveness of the proposed method.

Additionally, Table 3 presents specific imaging metrics. Comparing the metrics of PSNR, SSIM, and GMS, the RMA_Uniform method consistently performs the worst across

all SNR levels. The proposed method under coprime sampling improves the PSNR by at least 5.58 dB compared to RMA_Uniform method, and when the SNR drops to −10 dB, it can enhance the PSNR by up to 16.94 dB, while also increasing the SSIM by around 0.8 and GMS by around 0.8.

Compared to the l_1_Sparse method, the proposed method further enhances the PSNR by approximately 2 dB, increases the SSIM by about 0.1, and improves GMS by about 0.003, demonstrating the superior robustness of our method against noise.

Table 3. PSNR, SSIM, and GMS of Test 1 results using different methods.

SNR	Method	PSNR	SSIM	GMS
−10	RMA_Uniform	15.72	0.021	0.150
	l_1_Sparse	30.67	0.623	0.984
	Proposed Method	32.66	0.815	0.988
0	RMA_Uniform	22.67	0.027	0.142
	l_1_Sparse	32.24	0.777	0.992
	Proposed Method	34.36	0.907	0.995
10	RMA_Uniform	26.85	0.054	0.149
	l_1_Sparse	30.37	0.787	0.991
	Proposed Method	33.56	0.896	0.994
20	RMA_Uniform	27.72	0.082	0.171
	l_1_Sparse	32.06	0.850	0.991
	Proposed Method	33.30	0.895	0.995

2. Resolution Analysis

In this section, we analyze the resolution of the above simulation experiment. For the simulation scenes and experimental parameters in Figure 6 and Table 2, the theoretical range resolution of the short-range imaging radar system is $\delta_r = c/2B = 0.375$ m, and the azimuth resolution of the radar can be calculated as $\delta_a = \lambda R/2L \approx 0.42$ m, where λ is the carrier wavelength, R is the distance from the target to the radar, and L is the length of the azimuth synthetic aperture. We measured the resolutions of three comparative methods: RMA_Uniform, l_1_Sparse, and the proposed method. The resolution was determined by calculating the 3 dB mainlobe width of the reconstructed point targets. We average the results from nine point targets to obtain the final resolution for each method.

The actual range resolutions for the three methods are 0.38 m, 0.2 m, and 0.23 m, and the azimuth resolutions are 0.47 m, 0.23 m, and 0.25 m, respectively. These quantitative results demonstrate the significant resolution improvement of the proposed method compared to traditional RMA approaches. The proposed method achieves resolution comparable to sparse sampling, highlighting its effectiveness while providing a more structured sampling pattern.

3.1.4. Experiment Result of Test 2 (Point Array with Varying Energy Levels)

This test involves three spherical metal targets with different scattering energies of −10 dBsm, −20 dBsm, and −30 dBsm, as shown in Figure 8b. The imaging scene extends 1 m along the azimuth direction and 2 m along the range direction, with the center of the scene located approximately 15 m from the radar. In the experiment, similarly, 27 repeated periods are used to synthesize an aperture of 323 d, around 5 m. The radar operates at a carrier frequency of 10 GHz with a bandwidth of 2 GHz. The used radar system is shown in Figure 8a. The radar parameters are summarized in Table 4.

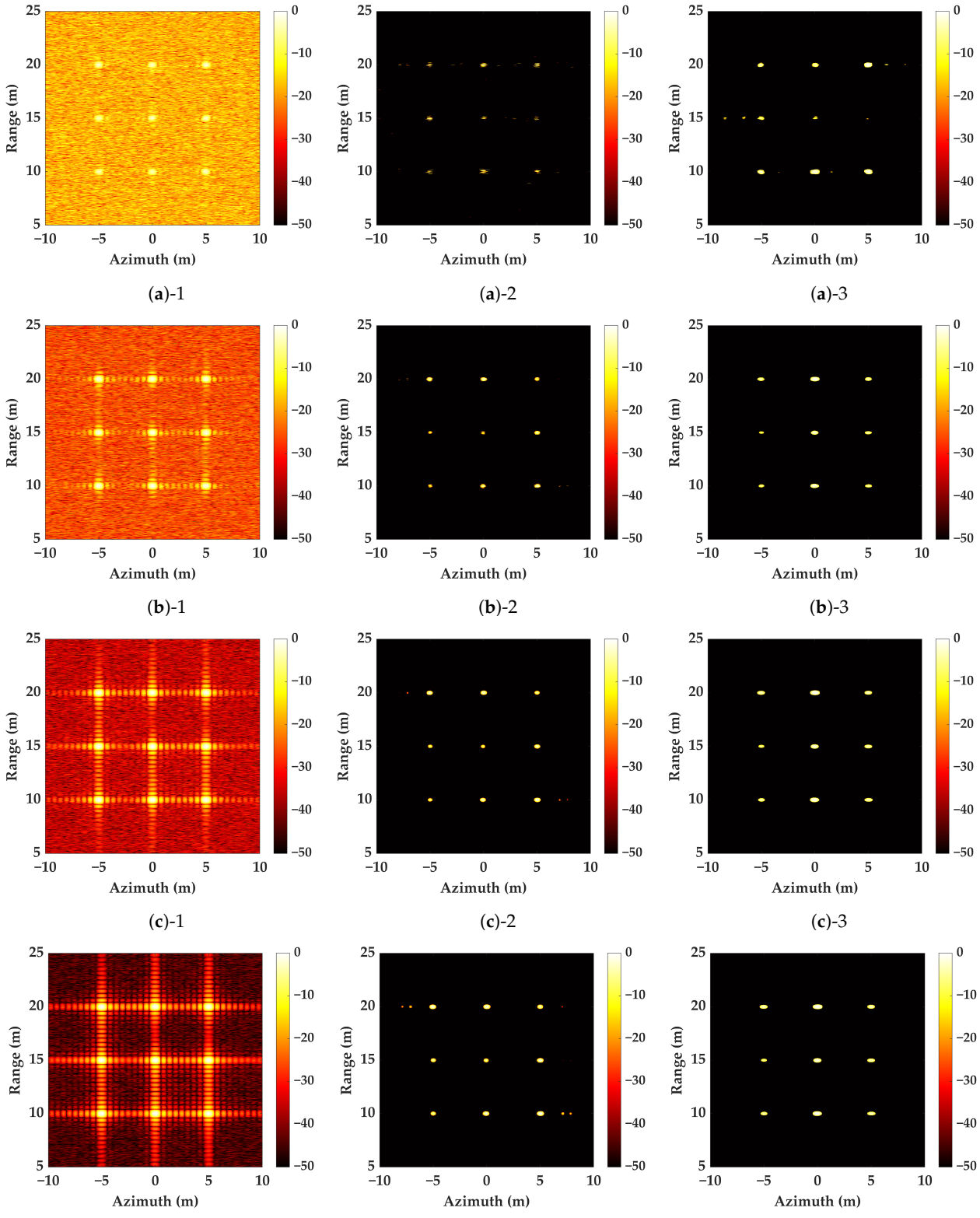
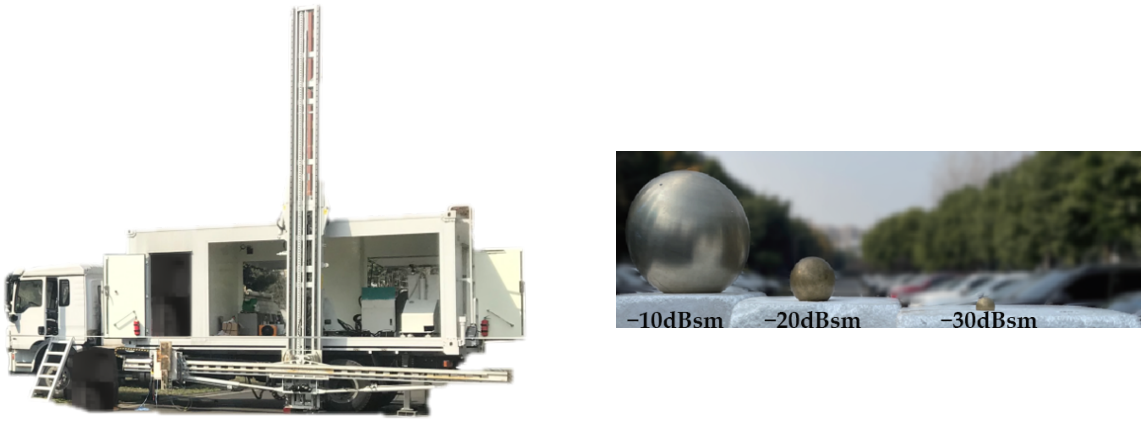


Figure 7. Imaging results for Test Scene 1 with SNR levels of −10 dB, 0 dB, 10 dB, and 20 dB from the first row to the last row, respectively. The columns show imaging results from RMA_Uniform, l_1_Sparse, and Proposed Method. The rows correspond to each SNR.

Table 4. Radar parameters.

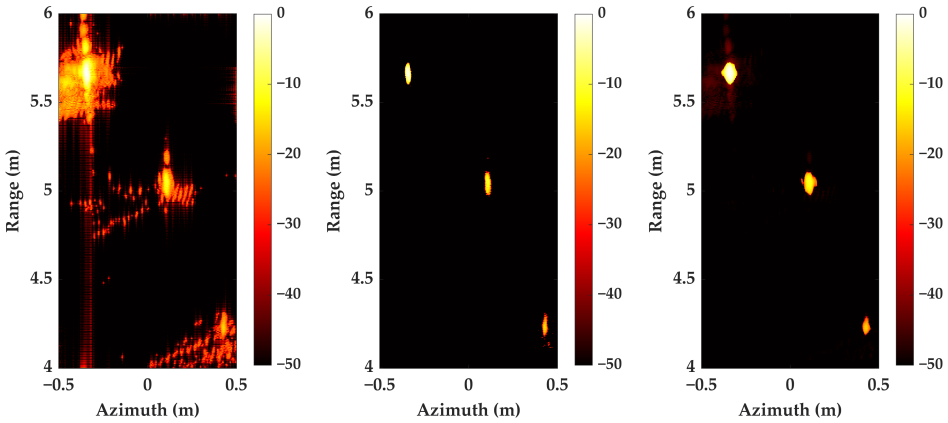
Parameters	Values
Carrier frequency	10 GHz
Bandwidth	2 GHz
Aperture length	5 m
Azimuth sampling points	163
Equivalent points	321



(**a**) (**b**)

Figure 8. The imaging system and scene of Test 2. (**a**) The microwave short-range imaging radar system used in Test 2 [7]. (**b**) Test 2: three point targets with varying energy levels.

In this set of experiments, we employ coprime sampling to synthesize an aperture 323d in length with 163 sampling points in the azimuth direction. Similarly, compared to uniform sampling with the same synthesized aperture length—which requires 13 equivalent phase centers—we only need 7 equivalent phase centers, reducing antenna resources by nearly half, as shown in Figure 3. Figure 9 presents the results obtained from the same imaging scenario using the three different methods previously described.



(**a**) (**b**) (**c**)

Figure 9. The imaging results of the point arrays with varying energy levels. (**a**) RMA_Uniform. (**b**) l_1_Sparse. (**c**) Proposed method.

It can be seen from Figure 9a that RMA_Uniform imaging clearly distinguishes the three spheres, with the energy levels of the spheres decreasing sequentially by around 10 dB. However, this method results in significant background clutter. Figure 9b shows the imaging results from l_1_Sparse, which avoids severe grating lobe interference and intense background clutter, enabling the clear distinction of the three targets with varying

energy levels. However, it also results in the loss of the targets' texture information. In contrast, Figure 9c shows the results obtained by the proposed method. Both background noise and grating lobe interference are effectively suppressed, providing a higher-precision representation of the three spheres. The texture information of the spherical targets is preserved, and the target energy is accurately estimated, demonstrating the effectiveness of the proposed method.

Additionally, Table 5 presents the specific imaging metrics for each method. It is noteworthy that the proposed method achieves the best results across all metrics, demonstrating its superior capability in achieving high-quality imaging for short-range radar imaging of simple spherical targets.

This test, similar to Test 1, focuses on point targets, but with a greater dynamic range among the targets. The energy levels of the three spheres differ significantly, resulting in a dynamic range of 20 dB between the strongest and weakest scatterers. This increased dynamic range makes the imaging task more challenging, especially for the preservation of weaker targets amidst stronger scatterers. As seen from the metrics, the proposed method not only effectively preserves the intensity differences between the targets but also maintains high robustness against noise, which is critical for the accurate interpretation of such complex scenarios. This result validates the effectiveness of our method in handling scenarios with larger dynamic variations compared to Test 1.

Table 5. PSNR, SSIM, and GMS of Test 2 with different methods.

Method	RMA_Uniform	l_1_Sparse	Proposed Method
PSNR	31.55	37.02	37.56
SSIM	0.275	0.796	0.947
GMS	0.919	0.985	0.988

3.1.5. Experiment Result of Test 3 (Controlled Layout with Complex Targets)

In this test, we increased the complexity of the imaging scenario by placing three different objects in the scene: a small cart, a metal frame, and an iron plate. The imaging scenario is shown in Figure 10b. The size of the imaging area is 4 m × 10 m, with the center of the scenario located 8 m away from the radar. The radar system used is shown in Figure 10a. To synthesize an aperture of length 1023d , equivalent to around 2 m, the radar was moved along the azimuth direction while forming 511 sampling points using a coprime sampling pattern. The carrier frequency of the radar is 78 GHz, with a bandwidth of around 4 GHz. The relevant radar parameters are summarized in Table 6.



(**a**) (**b**)

Figure 10. The imaging system and scene of Test 3. (**a**) The millimeter short-range imaging radar system used in Test 3. (**b**) Test 3: controlled layout with complex targets.

Table 6. Radar parameters.

Parameters	Values
Carrier frequency	78 GHz
Bandwidth	4 GHz
Aperture length	2 m
Azimuth sampling points	511
Equivalent points	1022

In this experiment, the complexity of the target layout aims to simulate a more realistic scenario compared to Tests 1 and 2. By including objects of different sizes, shapes, and material properties, this test evaluates the effectiveness of the imaging methods in capturing diverse target characteristics and preserving the spatial structure of complex scenes. Such conditions make it challenging to accurately reconstruct the imaging scene, especially when dealing with targets with different components.

The imaging results of this scenario are shown in Figure 11. The three targets are marked with white borders. Consistent with the experimental results from previous scenarios, the traditional RMA imaging method exhibits severe interference, including grating lobes and clutter, and shows weak robustness against noise. The l_1_Sparse method under sparse sampling results in many discrete strong scatterers, leading to the loss of target profile and texture information, thus performing poorly in terms of imaging accuracy and preservation of structural integrity.

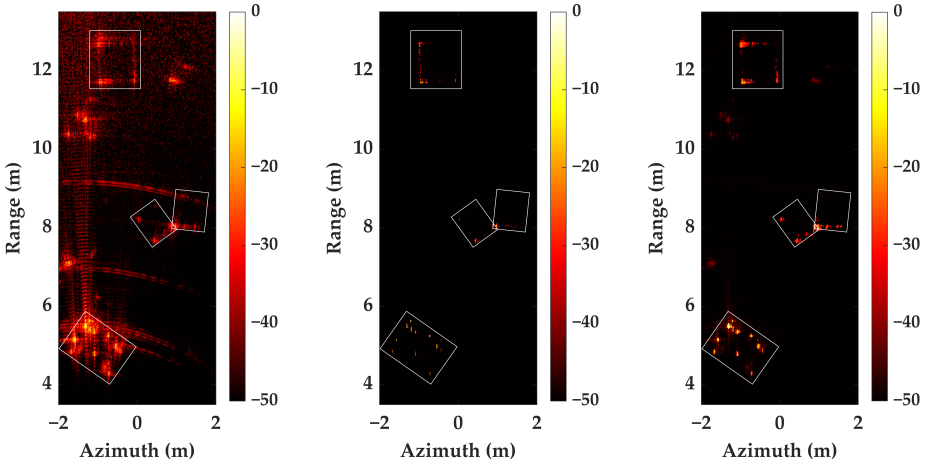


Figure 11. The imaging results of the controlled layout with complex targets. (**a**) RMA_Uniform. (**b**) l_1_Sparse. (**c**) Proposed method.

In contrast, the proposed method achieves a more complete target profile and demonstrates significant advantages in robustness to noise, imaging accuracy, and preservation of structural integrity.

Figure 12 presents the details of the imaging results for these three targets. Figure 12(a)-1–4 show the optical image of the iron plate and the radar images produced by the three different methods mentioned earlier. From Figure 12(a)-2, which corresponds to the RMA_Uniform method, it can be observed that the backscattered echoes from the edges and corners of the iron plate have strong scattering energy, which allows the main contours to be clearly presented in the radar image. Figure 12(a)-3, representing the l_1_Sparse method, effectively suppresses background clutter but fails to accurately present the target contour due to the inconsistent reconstruction of weaker scatterers.

In contrast, Figure 12(a)-4, which shows the results of the proposed method, demonstrates higher imaging quality compared to the others. The target contour is clearly visible, and both clutter and grating lobe interference are significantly reduced, providing a more

accurate representation of the iron plate. This improved clarity and reduction in unwanted artifacts highlight the superior capability of the proposed method in preserving structural details and mitigating noise effects in the imaging process.

Figure 12(b)-1–4 present the optical and radar images of the metal frame. The radar images reveal that the thinner column parts of the metal frame exhibit very weak scattering energy, making them difficult to reconstruct accurately. However, the main structure of the metal frame is reasonably well presented by some methods. Figure 12(b)-2, corresponding to RMA_Uniform, still suffers from significant noise interference and clutter, resulting in a loss of target detail and making the overall structure less discernible. Figure 12(b)-3, which shows the results of the l_1_Sparse, fails to retain the general shape of the target due to inconsistencies in scatterer reconstruction, especially in the weaker parts.

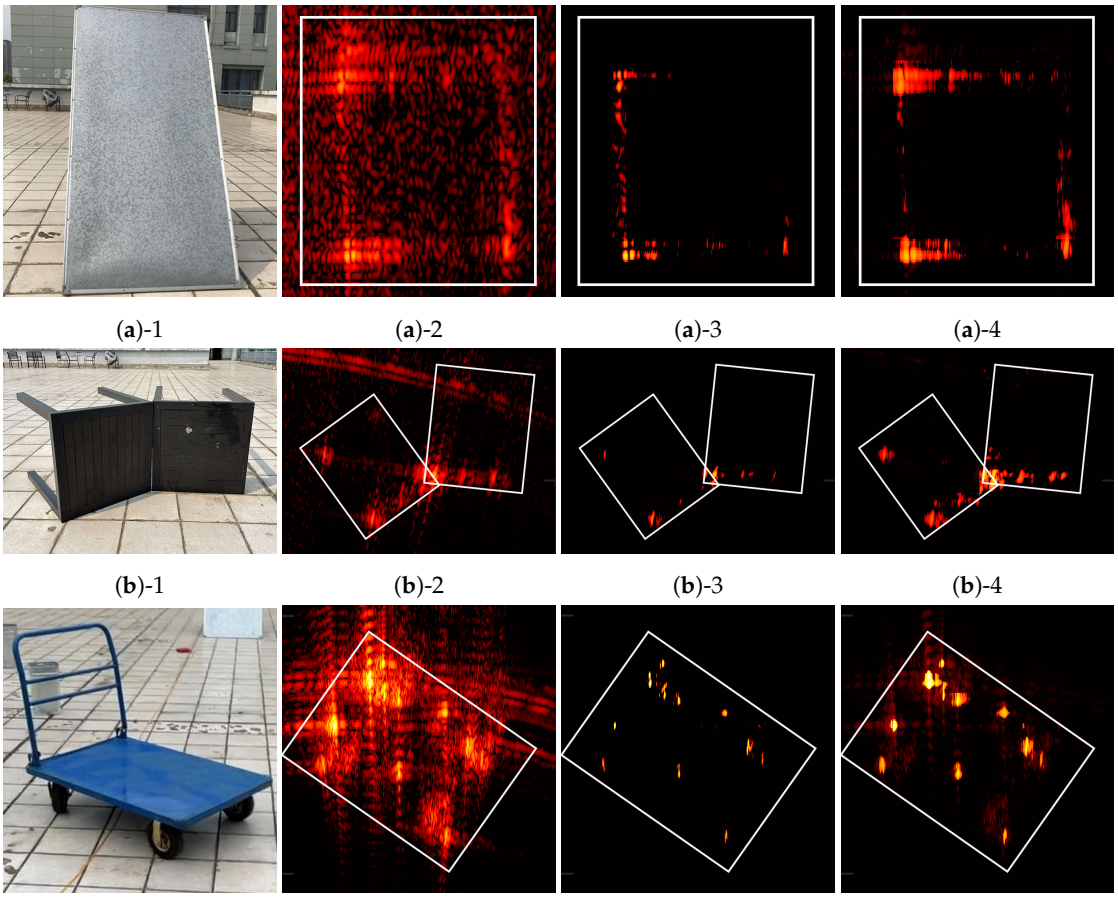


Figure 12. The imaging results of the targets in Test 3. From top to bottom: target 1 (the iron plate), target 2 (the metal frame), and target 3 (the small cart). The columns show the optical/radar images and the results from RMA_Uniform, l_1_Sparse, and the proposed method. The rows correspond to each target.

In contrast, Figure 12(b)-4, which presents the results of the proposed method, shows notable improvement in imaging quality. The clutter and grating lobe interference are significantly suppressed, allowing the main structure of the metal frame to be accurately represented. Although the thinner columns are still challenging to fully capture due to their weak scattering, the proposed method provides the clearest overall structure compared to other methods. These results highlight the superior capability of the proposed method in preserving structural integrity, even in scenarios involving weak scatterers and complex target configurations.

For the final target, the small cart consists of many discrete strong scatterers, and the effectiveness of the proposed method is clearly verified in the last row of imaging

results in Figure 12. The traditional RMA method fails to clearly represent the structure of the cart. The strong scatterers appear highly fragmented and significant background clutter is present, making it difficult to distinguish the true spatial distribution of the target. The l_1_Sparse method also struggles in this scenario, as the scatterers are inconsistently reconstructed, leading to a loss of the overall profile of the cart.

In contrast, the proposed method shows a more coherent reconstruction, capturing both the strong scatterers and the general shape of the small cart effectively. The background clutter is significantly suppressed, and the spatial arrangement of the scatterers is maintained, which helps in preserving the integrity of the cart's structure.

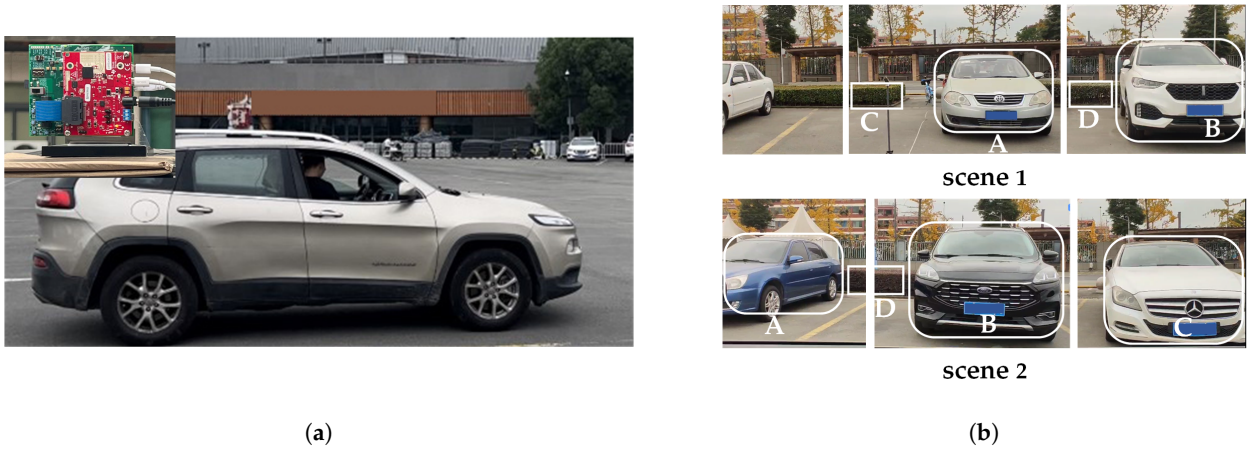
Table 7 lists the imaging metrics for the entire scenario using various methods. The PSNR values for RMA_Uniform, l_1_Sparse and the proposed method are 43.55, 47.99, and 46.98, respectively, with the proposed method outperforming the RMA_Uniform method by approximately 3 dB. Although the l_1-Sparse method achieves the highest PSNR metric, the proposed method is only 1 dB lower. Moreover, in other experimental scenarios, the proposed method consistently achieves the highest metrics. This still demonstrates the superiority of the proposed method in producing high-quality imaging results. Furthermore, the proposed method achieves the highest metric in SSIM and GMS, which indicates the best structural reconstruction of the image.

Table 7. PSNR, SSIM, and GMS of Test 3 with different methods.

Method	RMA_Uniform	l_1_Sparse	Proposed Method
PSNR	43.55	47.99	46.98
SSIM	0.289	0.815	0.938
GMS	0.518	0.957	0.966

3.1.6. Experiment Result of Test 4 (Real-World Parking Lot Scenario)

In the final test, we conducted an experiment in a real-world parking lot scenario, shown in Figure 13b, with the center of the scene located 8 m away from the radar. The size of the imaging area is 13 m × 10 m. A longer aperture is synthesized by moving the radar in the azimuth direction. Two segments of data are selected from this for imaging, and in each segment, the length of the synthesized aperture is 0.2 m, with 103 sampling points in the azimuth direction. The specific radar parameters are listed in Table 8. The radar system used is shown in Figure 13a.



(**a**) (**b**)

Figure 13. The imaging system and scene of Test 4. (**a**) The millimeter short-range imaging radar system used in Test 4. (**b**) Test 4: real-world parking lot scenario. And boxes A, B, C and D indicate the main targets in the scenes.

Table 8. Radar parameters.

Parameters	Values
Carrier frequency	78 GHz
Bandwidth	4 GHz
Aperture length	0.2 m
Azimuth sampling points	103
Equivalent points	204

Figure 14 presents the experimental results of the first segment of measured data. It is evident from the results that the proposed method has distinct advantages in terms of image quality. To analyze the details of the imaging results, we have highlighted the main targets in the scene using bounding boxes. Boxes A and B indicate the two cars in the parking lot. By examining the reconstruction of the targets within these boxes, it can be seen that the RMA_Uniform method roughly captures the target contours and structural features. However, there is significant clutter in the background, which blends with weaker target edges, such as the side edges of cars, weakening the contour information and reducing clarity. Additionally, the strong background clutter significantly impacts imaging accuracy and quality.

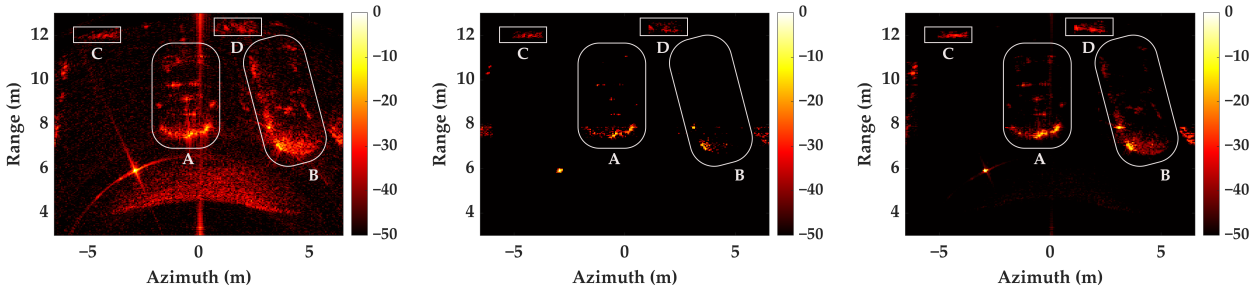


Figure 14. The imaging results of the first scene. (**a**) RMA_Uniform. (**b**) l_1_Sparse. (**c**) Proposed method.

In Figure 14b, which represents the l_1_Sparse method, there is a reduction in grating lobes compared to Figure 14a, but only the strong scattering points remain. Furthermore, some target contour information within Box B is filtered out, resulting in an incomplete representation of the target.

In contrast, Figure 14c, which shows the results of the proposed method, achieves higher precision with more complete target structures, offering the best imaging quality among the three methods. The target contours are clearly defined, and background clutter is effectively suppressed, allowing for a more accurate depiction of the vehicles.

Boxes C and D highlight the shrubbery in the parking lot, which has weak scattering energy and a short extent in the range direction. In the results of Figure 14a,b, the shrubbery is either obscured by background clutter or reconstructed as isolated points, failing to retain the true structure. However, the results from Figure 14c using the proposed method manage to preserve the complete structure of the shrubbery while effectively mitigating noise. This demonstrates the superior capability of the proposed method in reconstructing weak scatterers with complex backgrounds.

The PSNR, SSIM, and GMS metrics for this scenario are listed in Table 9. The proposed method outperforms the l_1_Sparse method by approximately 3 dB, indicating a significant improvement in the signal-to-noise ratio. And the proposed method achieves the highest SSIM, which reflects better structural similarity to the reference image. The GMS values show that the proposed method also has the highest metric, which further validates its superiority in preserving structural information and mitigating noise in the imaging results.

Table 9. PSNR, SSIM, and GMS of the first scene with different methods.

Method	RMA_Uniform	l_1_Sparse	Proposed Method
PSNR	40.44	46.19	49.35
SSIM	0.414	0.665	0.937
GMS	0.753	0.965	0.987

Figure 15 presents the imaging results of another segment of measured data, where Boxes A, B, and C represent three vehicles in the parking lot, and Box D highlights the shrubbery present in the scene. The imaging results obtained from RMA_Uniform, l_1_Sparse, and the proposed method are shown in Figures 15a, 15b, and 15c, respectively.

By analyzing the imaging accuracy and structural integrity of the image contours, it is evident that the proposed method provides the highest imaging quality. In Figure 15a, corresponding to RMA_Uniform, the vehicle contours are visible, but there is significant background clutter that mixes with weaker parts of the vehicles, such as side edges and less prominent features. This mixing weakens the clarity of the target contours, resulting in a reduction in the overall imaging accuracy.

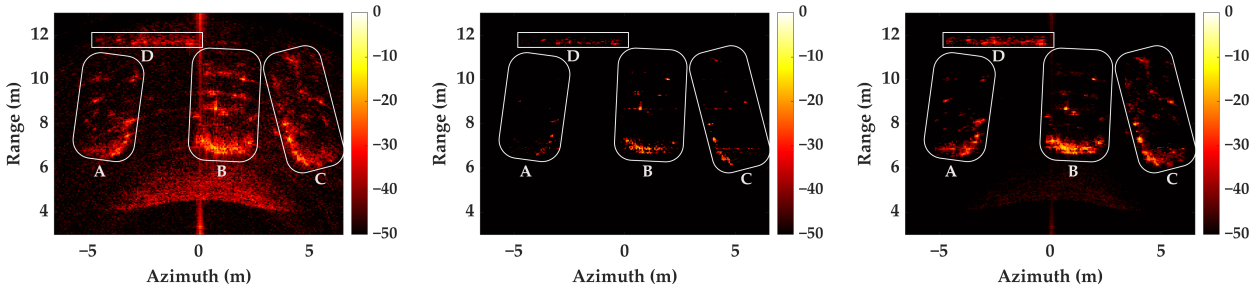


Figure 15. The imaging results of the second scene. (**a**) RMA_Uniform. (**b**) l_1_Sparse. (**c**) Proposed method.

Figure 15b, using the l_1_Sparse method, shows some improvement in reducing grating lobes compared to RMA_Uniform, but only the isolated strong scattering points remain. Some portions of the vehicles, particularly those in Boxes A and C, are either incorrectly reconstructed or filtered out, leading to a fragmented representation. Additionally, the shrubbery in Box D appears as a series of isolated points rather than a continuous structure, indicating that weak scatterers are not well preserved.

In contrast, Figure 15c, which shows the results of the proposed method, demonstrates significantly better imaging quality. The contours of all three vehicles are clearly reconstructed, with minimal background clutter. The proposed method effectively suppresses grating lobe interference, allowing for a clear distinction between the vehicles and the surrounding area. Additionally, the structural details of the shrubbery in Box D are well preserved, appearing as a continuous structure rather than isolated scatterers. This capability to reconstruct both strong and weak scatterers accurately highlights the robustness of the proposed method in maintaining both target integrity and image quality.

Table 10 lists the metrics of the imaging results for this scenario. The PSNR metrics indicate that the proposed method achieves the highest signal-to-noise ratio, outperforming the l_1_Sparse method by approximately 1.3 dB. And the proposed method achieves the highest SSIM, which reflects its superior ability to preserve the structural similarity of the scene compared to the reference. The GMS values demonstrate that the proposed method maintains the sharpness and structural integrity of the image, particularly in complex scenes with weak scatterers. Overall, the proposed method demonstrates its effectiveness in providing high-quality imaging with minimal interference and accurate structural reconstruction.

Table 10. PSNR, SSIM, and GMS of the second scene with different methods.

Method	RMA_Uniform	l_1_Sparse	Proposed Method
PSNR	41.39	46.02	47.37
SSIM	0.375	0.621	0.951
GMS	0.745	0.972	0.950

3.2. Ablation Study

In this section, we conduct an ablation study on the proposed method to validate the effectiveness of each of its components. Our proposed method is built on three core perspectives: physical sampling, equivalent signal measurement, and scene reconstruction. Among these, physical sampling refers to the actual radar sampling pattern, while equivalent signal measurement and scene reconstruction are components of the proposed imaging algorithm. In the ablation study, we focus on verifying the signal measurement and scene reconstruction components of the imaging method, indicating the effectiveness of the proposed processing method.

We perform a series of incremental experiments, where each core component is selectively excluded, and the resulting performance is compared with the method of the complete modules. Specifically, the first row of Table 11 represents the three core concepts of the proposed method, while the subsequent three rows correspond to the three methods included in the ablation study. In the table, check marks (✓) and crosses (✗) are used to indicate the presence or absence of each component in the respective methods. These three methods are introduced as follows:

1. Method 1: Range Migration Algorithm with Coprime Sampling (RMA_Coprime)
   This method applies the range migration algorithm to coprime sampling conditions, operating on the raw measured signal domain.
2. Method 2: Range Migration Algorithm with Equivalent Measurement from Coprime Sampling (RMA_Equivalent)
   This method utilizes the range migration algorithm to the equivalent measurement signal from coprime sampling, implementing it in the equivalent domain of the measured signal.
3. Method 3: Proposed Method
   The proposed method operates in the equivalent domain of the measured signal, focusing on both strong point scatterers and background textures to achieve a more comprehensive reconstruction.

Table 11. Ablation study on component contributions.

Method	Physical Sampling	Equivalent Signal Measurement	Scene Reconstruction
RMA_Coprime	✓	✗	✗
RMA_Equivalent	✓	✓	✗
Proposed Method	✓	✓	✓

We select the most complex parking lot scenario for the ablation study, specifically Scenario 1 in Test 4. The ablation results are shown in Figure 16.

Figure 16a, which shows the results of the RMA_Coprime method, exhibits strong grating lobe interference, where severe lobes drown out the target contours, making the targets nearly indistinguishable. In Figure 16b, which represents the RMA_Equivalent method, the severe grating lobes are eliminated, leaving more uniformly distributed clutter and sidelobes that are more easily suppressed through sparsity based methods. However, if we adopt the sparsity-based method directly in the raw measured data, the strong grating lobes cannot be filtered out. In conclusion, compared with the experimental results of the

first and second methods, the equivalent signal measurement component can help with the suppression of the grating lobes.

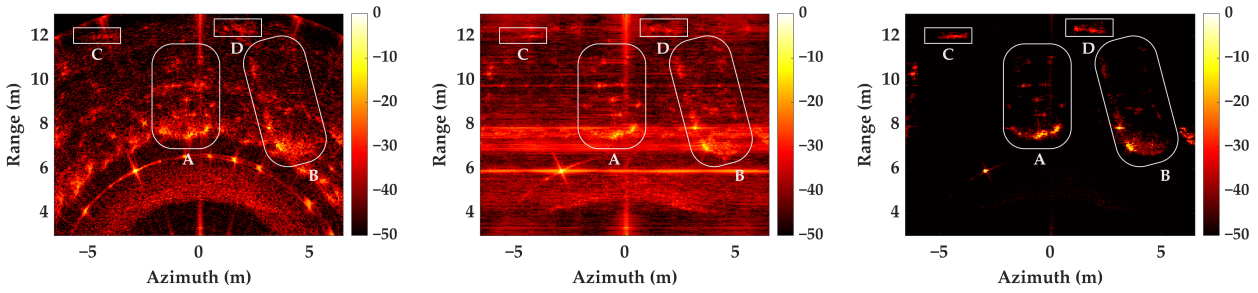


Figure 16. The imaging results of the first scene in Test 4. (**a**) RMA_Coprime. (**b**) RMA_Equivalent. (**c**) Proposed method.

Then, we compare the results of the proposed method with the other two methods. Figure 16c successfully suppresses the intense grating lobes and clutter interference while preserving the structure and texture details of the targets, delivering the most complete and high-quality imaging results. By incorporating all three core components, Figure 16c demonstrates the effectiveness of equivalent signal measurement and scene reconstruction when compared to Figure 16a. Additionally, when comparing it with Figure 16b, the remaining clutter and sidelobes in the imaging results are significantly reduced with the proposed component of the scene reconstruction. This highlights the critical importance of the scene reconstruction component.

Table 12 presents the results of the three methods involved in the ablation study in terms of PSNR, SSIM, and GMS imaging metrics. The results clearly show that the proposed method, which incorporates all three core components, achieves the highest metrics, thereby demonstrating its effectiveness. In contrast, RMA_Equivalent has the lowest imaging metrics and shows no improvement over RMA_Coprime, which is because significant clutter remains in the imaging results. However, as observed from the visualization results in Figure 16a,b, the equivalent signal measurement component effectively reduces grating lobe interference, facilitating the reconstruction of higher-quality imaging results.

Table 12. PSNR, SSIM, and GMS of the first scene with different methods.

Method	RMA_Coprime	RMA_Equivalent	Proposed Method
PSNR	40.44	35.29	49.35
SSIM	0.414	0.130	0.937
GMS	0.753	0.624	0.987

3.3. Computational Complexity Analysis

In this section, we analyze the computational complexity of the proposed method. Specifically, we analyze the computational complexity of the three comparative methods. Assuming M_r represents the number of imaging grids in the range direction and N_a represents the number of imaging grids in the azimuth direction. As all methods have the processing in the range direction, our analysis focuses primarily on the computational complexity of processing in the azimuth direction.

1. RMA_Uniform:
   For the RMA with uniform sampling, the primary computational steps involve FFT and IFFT operations. Consequently, the computational complexity of RMA_Uniform is mainly determined by performing 2D FFT and IFFT on a matrix of size $M_r \times N_a$, resulting in a complexity of $\mathcal{O}(M_r N_a \log_2 N_a)$.
2. l_1_Sparse:

For sparse sampling based on sparsity regularization, we assume the sampled points in the azimuth direction is K. The reconstruction process consists of iterations of two steps: gradient descent and soft-thresholding. The computational complexity of gradient descent is $\mathcal{O}(KM_rN_a)$ and that of soft-thresholding is $\mathcal{O}(M_rN_a)$. Assuming the algorithm requires I iterations, the overall computational complexity of sparse sampling is $\mathcal{O}(IKM_rN_a)$.

3. Proposed Method:
The proposed method consists of two parts: equivalent measured signal construction and scene reconstruction. Therefore, the computational complexity is analyzed for these two components:
(1) Equivalent measured signal construction: the main computational cost in this part arises from the calculation of the covariance matrix. For the echo matrix Y with dimensions $K \times M_r$, the computation of YY^H has a complexity of $\mathcal{O}(K^2M_r)$. Additionally, operations such as zero-padding the matrix and averaging the non-zero diagonal elements have a complexity of $\mathcal{O}(KM_r)$, which is negligible compared to $\mathcal{O}(K^2M_r)$. As a result, the computational complexity of this part is $\mathcal{O}(K^2M_r)$.
(2) Scene reconstruction: Similarly, for the part of scene reconstruction, it consists of iterations of different steps. Notably, instead of performing matrix multiplications at each iteration, we transform these operations into a combination of FFT, IFFT, and a multiplication with the extraction matrix, as shown in Equation (17). The computational complexity of the scene reconstruction part is primarily determined by the FFT operation and multiplication with the extraction matrix. The complexity of performing FFT on a matrix of size $M_r \times N_a$ is $\mathcal{O}(M_rN_a\log_2 N_a)$. The multiplication with the extraction matrix extracts K rows from the FFT-transformed matrix, with a complexity of $\mathcal{O}(KM_r)$, which is negligible compared to FFT. Assuming the processing iterates I times, the overall complexity of the scene reconstruction is $\mathcal{O}(IM_rN_a\log_2 N_a)$.
In summary, since multiple iterations are needed, the complexity of the first part $\mathcal{O}(K^2M_r)$ becomes negligible compared to the second part. Therefore, the total complexity of the proposed algorithm is $\mathcal{O}(IM_rN_a\log_2 N_a)$.

In summary, the computational complexity analysis highlights key differences between the methods. RMA_Uniform has the lowest complexity, $\mathcal{O}(M_rN_a\log_2 N_a)$, due to simple FFT and IFFT operations, making it efficient for uniform sampling. l_1_Sparse has a higher complexity, $\mathcal{O}(IKM_rN_a)$, due to iterative gradient descent and soft-thresholding. The proposed method achieves an efficiency improvement, $\mathcal{O}(IM_rN_a\log_2 N_a)$, by effectively combining FFT operations and extraction matrix multiplications. This balance ensures high efficiency while handling non-uniform or sparse data.

Additionally, we conducted a real-time performance test in Scenario 1 of Test 4, with the results presented in Table 13. From the results, it can be observed that the traditional RMA imaging method has the shortest runtime, while the sparse sampling approach requires the longest due to extensive matrix multiplication computations. In contrast, the proposed method achieves a runtime shorter than that of the sparse sampling method, demonstrating its relative advantage in terms of computational efficiency.

Table 13. Computational complexity analysis.

Method	Computational Complexity	Runtime
RMA_Uniform	$\mathcal{O}(M_rN_a\log_2 N_a)$	0.09 s
l_1_Sparse	$\mathcal{O}(IKM_rN_a)$	1.1 s
Proposed Method	$\mathcal{O}(IM_rN_a\log_2 N_a)$	0.8 s

4. Discussion

In this section, we systematically discuss the principles, practical implementations, and comparative advantages of coprime sampling, followed by an exploration of advanced signal processing strategies and future extensions. We begin by examining the practical

implementations and analyze coprime sampling in comparison with randomly sparse sampling methods. Moving forward, we discuss robust scene reconstruction techniques leveraging equivalent signal processing, with a particular focus on preserving background textures. Finally, we explore the potential for extending coprime sampling to 3D imaging scenarios.

4.1. Practical Implementations of Coprime Sampling

Our experiments were conducted on four test scenes using multiple periods of a basic coprime sampling pattern, with coprime numbers set to 3 and 5, as illustrated in Figure 3. The rationale for employing multiple periods of a basic coprime sampling unit is tied to improving imaging quality, particularly resolution—a central focus of recent research. From a resource efficiency perspective, even a single period of coprime sampling can enhance imaging quality when sampling resources are limited. However, the quality gains achieved with a single period are not comparable to those with multiple periods. With the shorter aperture length of a single period, targets in the scene are likely to deteriorate into individual scatterers due to lower resolution. Therefore, we prefer the approach of multiple periods of coprime sampling.

For the last three sets of measured data, we acquired the original data through motion synthesis with a single antenna (Test 2) or a MIMO antenna array (Tests 3 and 4), forming a uniform sampling pattern. These systems were not initially designed for such experiments. To align with our study's objectives, we extracted the experiment data from the original measurements following the coprime sampling pattern based on the equivalent phase center principle.

A key future goal remains to develop a dedicated system capable of direct coprime sampling. Physically implementing such sampling patterns presents two primary options: (1) cascading multiple multichannel arrays, where each array represents a basic coprime unit, or (2) motion synthesis of a single array. The former requires a larger installation space and is more suitable for platforms such as vehicles or rail-based systems, while the latter may be more fitting for platforms like robots or unmanned aerial vehicles. In practice, challenges such as maintaining channel balance and achieving precise motion compensation are crucial aspects that may impact the system's reliability and accuracy. Channel-balancing issues could arise due to mismatched gain and phase responses among different channels, leading to image artifacts and decreased resolution [63,64]. Motion-compensation challenges stem from the need to precisely align the movement of sensors or antennas, as even small inaccuracies can distort the reconstruction [65]. Addressing these challenges is essential for ensuring consistent performance. Thus, a deeper investigation into robust calibration and compensation methods would be an important direction for future research.

4.2. More Advanced Layouts of Coprime Sampling

As illustrated in Figure 3, the entire layout of the coprime sampling pattern comprises two sub-patterns, corresponding to the two coprime numbers, 3 and 5, respectively. In this arrangement, the first sampling point located at position $0d$ is shared by both sub-patterns. This configuration can also be interpreted as the two sub-patterns being aligned head-to-head, often referred to as the prototype coprime configuration in traditional array signal processing contexts.

From the perspective of sub-pattern displacement, there is no offset between the two patterns in this configuration. However, more generalized layouts of coprime sampling can be realized by introducing adjustments to the displacement between the two sub-patterns [42]. This opens up possibilities for diversifying the overall sampling patterns, which remains an area of potential exploration in future work.

4.3. Comparison with Randomly Sparse Sampling

From a resource efficiency perspective, coprime sampling allows us to achieve high-quality imaging results while conserving about 50% of sampling resources. This approach balances resource utilization and image quality effectively. Although current randomly sparse sampling strategies may offer greater resource savings [3,6,12], these advantages are often outweighed by implementation challenges. As discussed earlier, random sampling patterns can complicate hardware design and implementation, increasing system complexity. In contrast, coprime sampling provides a structured approach that maintains regularity, enabling more straightforward system design and implementation while still offering substantial resource savings. This trade-off between resource efficiency and practical implementation makes coprime sampling an attractive option for short-range radar imaging.

4.4. Background Texture-Preservation Strategies

In the design of the scene reconstruction method, preserving the background texture around the target is a priority to facilitate the interpretation of imaging results in short-range radar scenarios. These background textures often provide weak contours that supplement the information of strong scatterers in the domain. Our current approach for background texture preservation involves a dedicated modification of the reconstruction steps based on the original proximal-gradient algorithm, which utilizes an l_1-based sparsity regularization term.

Looking forward, more targeted regularization terms can be incorporated to specifically preserve background textures. For instance, given that continuity, smoothness, and regularity are common characteristics of background textures (often forming regular geometric patterns like lines and planes), mathematical regularizers such as the total-variation norm or low-rank norm could be introduced [38,39,66]. This would help in forming a new optimization problem for scene reconstruction, solved using methods like the Alternating Direction Method of Multipliers (ADMM) [56].

However, compared to the current l_1-based sparsity regularization term, these approaches could significantly slow down the solving process. A promising alternative could be exploring the integration of regularization capabilities derived from deep neural networks to enhance both the efficiency and effectiveness of texture preservation in future work.

4.5. Another Perspective for Equivalent Measured Signal Processing

In this study, we establish an equivalent forward measurement process by utilizing the second-order statistical information of the original measured signal. This equivalent signal encapsulates the energy distribution of the target within the imaging scene, enabling us to form a sparsity-based regularization model for imaging. However, it is worth considering that there may be alternative methods to process this equivalent signal.

One such alternative involves addressing the missing data points, or "holes", in the equivalent measured signal. These missing points result from the non-uniformity compared to a fully uniformly sampled signal. A possible approach is to treat these holes as an optimization problem, employing low-rank properties as a regularization term to fill in the gaps and obtain an equivalent signal with a uniform sampling pattern [67–70]. Once filled, this completed signal can be processed using traditional matched-filter-based scene reconstruction methods like RMA.

However, we choose not to pursue this two-step approach for several reasons. Firstly, solving the optimization problem to fill the holes efficiently is computationally intensive and challenging. Secondly, after filling the holes, traditional matched-filter-based methods inevitably introduce non-ideal factors, such as sidelobes, which can degrade the imaging quality. Therefore, instead of this two-step process, we adopt a one-step approach where we directly use the equivalent measured signal to reconstruct the scene.

An additional factor to consider is the reliability of the equivalent signal obtained through covariance matrix estimation. In theory, estimating the covariance matrix requires a large number of samples to achieve high accuracy. In practice, however, the number of available samples is often limited. In our study, we mitigate this limitation by leveraging local similarities in adjacent range units and exploiting the diagonal samples' correlation in the covariance matrix. Even with these measures, there are unavoidable errors in the estimation, resulting in a noisy equivalent measured signal.

Given the inherent noise and errors in the equivalent signal, adopting a regularization-based imaging model with a sparsity regularization term becomes more advantageous. Such a model offers better resistance to noise and can handle the inaccuracies in the equivalent signal more effectively than traditional methods. This rationale underpins our decision to use the one-step processing approach in this study.

4.6. Extending Coprime Sampling to 3D Imaging Scenarios

It is natural to extend coprime sampling to 3D imaging scenarios, which could offer even more significant benefits compared to the current 2D case. Current 3D imaging typically relies on a 2D imaging aperture, where the additional dimension is often formed through time-consuming motion synthesis [11]. By adopting coprime sampling, we could potentially reduce the required sampling points in this dimension by approximately half, significantly decreasing imaging time and enabling higher imaging frame rates.

4.7. Extending Coprime Sampling to Complex Environments

Our study is currently preliminary, focusing mainly on introducing coprime sampling to short-range radar imaging. In real-world applications, dynamic environments present additional challenges to the imaging process. Moving targets, for example, can cause Doppler shifts that lead to phase errors in the measured signal. These errors distort the equivalent signal and affect imaging results. To address this, we could explore advanced signal processing techniques like motion compensation and phase error correction to enhance the imaging method's robustness in dynamic scenarios [65]. Beyond dynamic environments, other challenges exist, such as the multi-path effect from the ground, which causes strong interference and clutter, adding complexity to the imaging process. Future research could integrate advanced signal processing techniques, including multi-view processing, to address these challenges and improve coprime sampling performance in complex environments [47]. Additionally, the imaging scene's swath warrants further study, as our current work focuses on a limited swath. Extending to a larger swath could provide more comprehensive imaging results through techniques like high-resolution and wide-swath SAR (HRWS-SAR) [71].

5. Conclusions

In this study, we explored the application of coprime sampling in short-range imaging radar to address the resource constraints and implementation challenges faced by traditional sampling techniques. Our approach leveraged the structured and resource-efficient nature of coprime sampling to extend the effective aperture size while minimizing the number of physical sampling elements. By forming a new equivalent measurement model based on second-order statistical information, we established a robust imaging framework that effectively balances target resolution, signal-to-noise ratio, and resource efficiency.

We demonstrated that coprime sampling offers a practical alternative to existing uniform and sparse sampling methods by creating a structured yet sparse pattern that simplifies implementation and enhances imaging performance. Additionally, our novel scene reconstruction approach successfully preserved background textures while enhancing target resolution, showcasing its potential for real-world short-range radar applications. Our experimental results validated the effectiveness of this method across various scenarios, revealing significant improvements in image quality and resolution compared to traditional techniques.

However, challenges like precise calibration, motion compensation, and handling noisy equivalent measurements warrant further investigation to ensure consistently high-quality results. Future directions include refining the measurement model for dynamic environments, integrating advanced regularization techniques for texture preservation, and extending coprime sampling to 3D scenarios, thereby enhancing the versatility and reliability of short-range radar systems in applications like autonomous navigation, security screening, and environmental monitoring.

Author Contributions: Conceptualization, X.Z. (Xu Zhan); Data curation, M.W. and S.W.; Formal analysis, Y.W. and X.Z. (Xu Zhan); Funding acquisition, T.Z., J.S. and X.Z. (Xiaoling Zhang); Investigation, Y.W. and X.Z. (Xu Zhan); Methodology, Y.W. and X.Z. (Xu Zhan); Project administration, T.Z. and X.Z. (Xiaoling Zhang); Resources, M.W. and S.W.; Supervision, X.Z., T.Z., J.S. and X.Z. (Xiaoling Zhang); Validation, Y.W.; Visualization, Y.W.; Writing—original draft, Y.W., X.Z. (Xu Zhan) and X.M.; Writing—review and editing, Y.W. and X.Z. (Xu Zhan). All authors have read and agreed to the published version of the manuscript.

Funding: This work was supported in part by the National Natural Science Foundation of China under Grants 62471113, 62305049 and 62371104, in part by Sichuan Science and Technology Program 2024NS-FSC0479 and 2024NS-FSC1439, and in part by Aeronautical Science Foundation of China 1A2024Z071080005.

Data Availability Statement: The datasets presented in this article are not readily available because the data are part of an ongoing study.

Conflicts of Interest: The authors declare no conflicts of interest.

References

1. Zeng, T.; Zhang, W.; Zhan, X.; Xu, X.; Liu, Z.; Wang, B.; Zhang, X. A Novel Multimodal Fusion Framework Based on Point Cloud Registration for Near-Field 3D SAR Perception. *Remote Sens.* **2024**, *16*, 952. [CrossRef]
2. Fu, J.; Xing, M.; Sun, G. Time-Frequency Reversion-Based Spectrum Analysis Method and Its Applications in Radar Imaging. *Remote Sens.* **2021**, *13*, 600. [CrossRef]
3. Zeng, T.; Zhan, X.; Ma, X.; Liu, R.; Shi, J.; Wei, S.; Wang, M.; Zhang, X. Unsupervised 3D array-SAR imaging based on generative model for scattering diagnosis. *IEEE Antennas Wirel. Propag. Lett.* **2024**, *23*, 2451–2455. [CrossRef]
4. Wang, Y.; Zhan, X.; Yao, J.; Gao, J.; Zhan, Y.; Bai, J. 3D sparse SAR imaging based on complex-valued nonconvex regularization for scattering diagnosis. *IEEE Antennas Wirel. Propag. Lett.* **2023**, *23*, 888–892
5. Zhan, X.; Zhang, X.; Shi, J.; Wei, S. Constant-Time-Delay Interferences in Near-Field SAR: Analysis and Suppression in Image Domain. In Proceedings of the IGARSS 2022—2022 IEEE International Geoscience and Remote Sensing Symposium, Kuala Lumpur, Malaysia, 17–22 July 2022; IEEE: Piscataway, NJ, USA, 2022, pp. 3436–3439.
6. Wang, Y.; Zhang, X.; Zhan, X.; Zhang, T.; Zhou, L.; Shi, J.; Wei, S. An RCS measurement method using sparse imaging based 3-D SAR complex image. *IEEE Antennas Wirel. Propag. Lett.* **2021**, *21*, 24–28. [CrossRef]
7. Zhan, X.; Zhang, X.; Shi, J.; Wei, S.; Zeng, T.; Pu, L. VehMIR: Vehicle-borne Mobile Imaging Radar for Scattering Imaging Measurement in the Near-field Region. In Proceedings of the 2023 IEEE Radar Conference (RadarConf23), San Antonio, TX, USA, 1–5 May 2023; IEEE: Piscataway, NJ, USA, 2023; pp. 1–6.
8. Pieraccini, M.; Miccinesi, L. Ground-based radar interferometry: A bibliographic review. *Remote Sens.* **2019**, *11*, 1029. [CrossRef]
9. Li, Y.; Xu, H.; Xu, J.; Chen, H.; An, Q.; Hou, K.; Wang, J. Design of a Near-Field Synthetic Aperture Radar Imaging System Based on Improved RMA. *Remote Sens.* **2024**, *16*, 3342. [CrossRef]
10. Xing, S.; Song, S.; Quan, S.; Sun, D.; Wang, J.; Li, Y. Near-field 3D sparse SAR direct imaging with irregular samples. *Remote Sens.* **2022**, *14*, 6321. [CrossRef]
11. Wei, S.; Zhou, Z.; Wang, M.; Wei, J.; Liu, S.; Shi, J.; Zhang, X.; Fan, F. 3DRIED: A high-resolution 3-D millimeter-wave radar dataset dedicated to imaging and evaluation. *Remote Sens.* **2021**, *13*, 3366. [CrossRef]
12. Wang, Y.; He, Z.; Zhan, X.; Zeng, Q.; Hu, Y. A 3-D sparse SAR imaging method based on plug-and-play. *IEEE Trans. Geosci. Remote Sens.* **2022**, *60*, 1–14. [CrossRef]
13. Wang, Y.; Zhan, X.; Gao, J.; Yao, J.; Wei, S.; Bai, J. Array SAR 3D Sparse Imaging Based on Regularization by Denoising Under Few Observed Data. *IEEE Trans. Geosci. Remote Sens.* **2024**, *62*, 5213114 .
14. Wang, Y.; He, Z.; Zhan, X.; Fu, Y.; Zhou, L. Three-dimensional sparse SAR imaging with generalized L q regularization. *Remote Sens.* **2022**, *14*, 288. [CrossRef]
15. Ludeno, G.; Antuono, M.; Soldovieri, F.; Gennarelli, G. A Feasibility Study of Nearshore Bathymetry Estimation via Short-Range K-Band MIMO Radar. *Remote Sens.* **2024**, *16*, 261. [CrossRef]
16. Zou, L.; Li, Y.; Alani, A.M. Pseudopolar Format Matrix Description of Near-Range Radar Imaging and Fractional Fourier Transform. *Remote Sens.* **2024**, *16*, 2482. [CrossRef]

17. Yan, Q.; Jiao, Z.; Qiu, X.; Wang, B.; Ding, C. Comparison between different TomoSAR imaging models for airborne platform flying at low altitude. *Remote Sens.* **2022**, *14*, 5452. [CrossRef]
18. Baffelli, S.; Frey, O.; Hajnsek, I. Geostatistical Analysis and Mitigation of the Atmospheric Phase Screens in Ku-Band Terrestrial Radar Interferometric Observations of an Alpine Glacier. *IEEE Trans. Geosci. Remote Sens.* **2020**, *58*, 7533–7556. [CrossRef]
19. Di Traglia, F.; De Luca, C.; Manzo, M.; Nolesini, T.; Casagli, N.; Lanari, R.; Casu, F. Joint exploitation of space-borne and ground-based multitemporal InSAR measurements for volcano monitoring: The Stromboli volcano case study. *Remote Sens. Environ.* **2021**, *260*, 112441. [CrossRef]
20. Baumann-Ouyang, A.; Butt, J.A.; Salido-Monzú, D.; Wieser, A. Mimo-sar interferometric measurements for structural monitoring: accuracy and limitations. *Remote Sens.* **2021**, *13*, 4290. [CrossRef]
21. Zhang, Z.; Li, Z.; Suo, Z.; Qi, L.; Tang, F.; Guo, H.; Tao, H. A Reliable Observation Point Selection Method for GB-SAR in Low-Coherence Areas. *Remote Sens.* **2024**, *16*, 1251. [CrossRef]
22. Xu, G.; Chen, Y.; Ji, A.; Zhang, B.; Yu, C.; Hong, W. 3-D High-Resolution Imaging and Array Calibration of Ground-Based Millimeter-Wave MIMO Radar. *IEEE Trans. Microw. Theory Tech.* **2024**, *72*, 4919–4931. [CrossRef]
23. Zhang, F.; Luo, C.; Fu, Y.; Zhang, W.; Yang, W.; Yu, R.; Yan, S. Frequency Domain Imaging Algorithms for Short-Range Synthetic Aperture Radar. *Remote Sens.* **2023**, *15*, 5684. [CrossRef]
24. Hua, Y.; Wang, J.; Feng, D.; Huang, X. A Novel 3D ArcSAR Sensing System Applied to Unmanned Ground Vehicles. *Remote Sens.* **2023**, *15*, 4089. [CrossRef]
25. Polisano, M.G.; Manzoni, M.; Tebaldini, S.; Monti-Guarnieri, A.; Prati, C.M.; Russo, I. Very high resolution automotive SAR imaging from burst data. *Remote Sens.* **2023**, *15*, 845. [CrossRef]
26. Guo, P.; Wu, F.; Tang, S.; Jiang, C.; Liu, C. Implementation Method of Automotive Video SAR (ViSAR) Based on Sub-Aperture Spectrum Fusion. *Remote Sens.* **2023**, *15*, 476. [CrossRef]
27. Manzoni, M.; Tebaldini, S.; Monti-Guarnieri, A.V.; Prati, C.M.; Russo, I. A comparison of processing schemes for automotive MIMO SAR imaging. *Remote Sens.* **2022**, *14*, 4696. [CrossRef]
28. Tebaldini, S.; Manzoni, M.; Tagliaferri, D.; Rizzi, M.; Monti-Guarnieri, A.V.; Prati, C.M.; Spagnolini, U.; Nicoli, M.; Russo, I.; Mazzucco, C. Sensing the urban environment by automotive SAR imaging: Potentials and challenges. *Remote Sens.* **2022**, *14*, 3602. [CrossRef]
29. Jiang, M.; Xu, G.; Pei, H.; Feng, Z.; Ma, S.; Zhang, H.; Hong, W. 4d high-resolution imagery of point clouds for automotive mmwave radar. *IEEE Trans. Intell. Transp. Syst.* **2023**, *25*, 998–1012. [CrossRef]
30. Xu, G.; Pei, H.; Jiang, M.; Chen, J.; Wang, H.; Zhang, H.; Liu, Y. High-resolution mmWave SAR imagery for automotive parking assistance. *IEEE J. Miniaturization Air Space Syst.* **2022**, *4*, 54–61. [CrossRef]
31. Xu, Y.; Zhang, X.; Wei, S.; Shi, J.; Zeng, T.; Xu, X.; Zhang, W.; Zhan, X. Joint Generalized Lq and Convolutional Regularization: Enhancing mmW Automotive SAR Sparse Imaging. *IEEE Trans. Geosci. Remote Sens.* **2024**, *62*, 1–15 . [CrossRef]
32. Cheng, Y.; Su, J.; Jiang, M.; Liu, Y. A novel radar point cloud generation method for robot environment perception. *IEEE Trans. Robot.* **2022**, *38*, 3754–3773. [CrossRef]
33. Li, S.; Wu, S. Low-cost millimeter wave frequency scanning based synthesis aperture imaging system for concealed weapon detection. *IEEE Trans. Microw. Theory Tech.* **2022**, *70*, 3688–3699. [CrossRef]
34. Feng, W.; Yi, L.; Sato, M. Near range radar imaging based on block sparsity and cross-correlation fusion algorithm. *IEEE J. Sel. Top. Appl. Earth Obs. Remote Sens.* **2018**, *11*, 2079–2089. [CrossRef]
35. Miran, E.A.; Oktem, F.S.; Koc, S. Sparse reconstruction for near-field MIMO radar imaging using fast multipole method. *IEEE Access* **2021**, *9*, 151578–151589. [CrossRef]
36. Simoni, R.; Mateos-Núñez, D.; González-Huici, M.A.; Correas-Serrano, A. Height estimation for automotive MIMO radar with group-sparse reconstruction. *arXiv* **2019**, arXiv:1904.09715.
37. Song, S.; Dai, Y.; Sun, S.; Jin, T. Efficient Image Reconstruction Methods Based on Structured Sparsity for Short-Range Radar. *IEEE Trans. Geosci. Remote Sens.* **2024**, *62*, 5212615 . [CrossRef]
38. Roldan, I.; Fioranelli, F.; Yarovoy, A. Total Variation Compressive Sensing for 3D Shape Estimation in Short-Range Imaging Radars. *IEEE Trans. Radar Syst.* **2023**, *1*, 583–592 . [CrossRef]
39. Tang, J.; Liu, Z.; Ran, L.; Xie, R.; Qin, J. Forward-Looking Super-Resolution Imaging of MIMO Radar via Sparse and Double Low-Rank Constraints. *Remote Sens.* **2023**, *15*, 609. [CrossRef]
40. Xu, G.; Zhang, B.; Yu, H.; Chen, J.; Xing, M.; Hong, W. Sparse synthetic aperture radar imaging from compressed sensing and machine learning: Theories, applications, and trends. *IEEE Geosci. Remote Sens. Mag.* **2022**, *10*, 32–69. [CrossRef]
41. Yang, J.; Li, W.; Li, K.; Chen, R.; Zhang, K.; Mao, D.; Zhang, Y. Sparse Bayesian Learning-based Multichannel Radar Forward-Looking Superresolution Imaging Considering Grid Mismatch. *IEEE J. Sel. Top. Appl. Earth Obs. Remote Sens.* **2024**, *17*, 14997–15008. [CrossRef]
42. Qin, S.; Zhang, Y.D.; Amin, M.G. Generalized coprime array configurations for direction-of-arrival estimation. *IEEE Trans. Signal Process.* **2015**, *63*, 1377–1390. [CrossRef]
43. Pal, P.; Vaidyanathan, P.P. Coprime sampling and the MUSIC algorithm. In Proceedings of the 2011 Digital Signal Processing and Signal Processing Education Meeting (DSP/SPE), Corfu, Greece, 6–8 July 2011; IEEE: Piscataway, NJ, USA, 2011; pp. 289–294.
44. Vaidyanathan, P.; Pal, P. Theory of sparse coprime sensing in multiple dimensions. *IEEE Trans. Signal Process.* **2011**, *59*, 3592–3608. [CrossRef]

45. Naghibi, A.; Attari, A.R. Near-field radar-based microwave imaging for breast cancer detection: A study on resolution and image quality. *IEEE Trans. Antennas Propag.* **2020**, *69*, 1670–1680. [CrossRef]
46. Hu, C.; Wang, J.; Tian, W.; Wang, R.; Li, H.; Zhu, L. Generalized ambiguity function properties of ground-based wideband MIMO imaging radar. *IEEE Trans. Aerosp. Electron. Syst.* **2018**, *55*, 578–591. [CrossRef]
47. Manzoni, M.; Tebaldini, S.; Monti-Guarnieri, A.V.; Prati, C.M. Multipath in automotive MIMO SAR imaging. *IEEE Trans. Geosci. Remote Sens.* **2023**, *61*, 1–12. [CrossRef]
48. Smith, J.W.; Torlak, M. Efficient 3-D near-field MIMO-SAR imaging for irregular scanning geometries. *IEEE Access* **2022**, *10*, 10283–10294. [CrossRef]
49. Wang, S.; Li, S.; Zhao, G.; Amin, M.G. Efficient wavenumber domain processing for near-field imaging with polyline arrays. *IEEE Trans. Microw. Theory Tech.* **2022**, *70*, 4544–4555. [CrossRef]
50. Li, S.; Wang, S.; An, Q.; Zhao, G.; Sun, H. Cylindrical MIMO array-based near-field microwave imaging. *IEEE Trans. Antennas Propag.* **2020**, *69*, 612–617. [CrossRef]
51. Zhan, X.; Zhang, X.; Ma, X.; Wei, S.; Shi, J.; Zeng, T. Recent Progress in Sparsity-Regularization Based Imaging Method for Near-Field 3D SAR. In Proceedings of the IGARSS 2023—2023 IEEE International Geoscience and Remote Sensing Symposium, Pasadena, CA, USA, 16–21 July 2023; IEEE: Piscataway, NJ, USA, 2023; pp. 1802–1805.
52. Zhang, X.; Zhan, X.; Ma, X.; Shi, J.; Wei, S.; Zeng, T. Solving 3d radar imaging inverse problems With a multi-cognition task-oriented framework. In Proceedings of the IGARSS 2023—2023 IEEE International Geoscience and Remote Sensing Symposium, Pasadena, CA, USA, 16–21 July 2023; IEEE: Piscataway, NJ, USA, 2023, pp. 7949–7952.
53. Di Martino, G.; Iodice, A. Coprime synthetic aperture radar (CopSAR): A new acquisition mode for maritime surveillance. *IEEE Trans. Geosci. Remote Sens.* **2014**, *53*, 3110–3123. [CrossRef]
54. Di Martino, G.; Iodice, A. Orthogonal coprime synthetic aperture radar. *IEEE Trans. Geosci. Remote Sens.* **2016**, *55*, 432–440. [CrossRef]
55. Jiao, Z.; Ding, C.; Qiu, X.; Zhou, L.; Chen, L.; Han, D.; Guo, J. Urban 3D imaging using airborne TomoSAR: Contextual information-based approach in the statistical way. *ISPRS J. Photogramm. Remote Sens.* **2020**, *170*, 127–141. [CrossRef]
56. Parikh, N.; Boyd, S. Proximal algorithms. *Found. Trends® Optim.* **2014**, *1*, 127–239. [CrossRef]
57. Hastie, T.; Tibshirani, R.; Wainwright, M. Statistical learning with sparsity. *Monogr. Stat. Appl. Probab.* **2015**, *143*, 8.
58. Lu, S.; Yuan, X.; Shi, W. Edge compression: An integrated framework for compressive imaging processing on cavs. In Proceedings of the 2020 IEEE/ACM Symposium on Edge Computing (SEC), San Jose, CA, USA, 12–14 November 2020; IEEE: Piscataway, NJ, USA, 2020; pp. 125–138.
59. Zhang, Z.; Zhang, B.; Yuan, X.; Zheng, S.; Su, X.; Suo, J.; Brady, D.J.; Dai, Q. From compressive sampling to compressive tasking: retrieving semantics in compressed domain with low bandwidth. *PhotoniX* **2022**, *3*, 19. [CrossRef]
60. Horé, A.; Ziou, D. Image Quality Metrics: PSNR vs. SSIM. In Proceedings of the 2010 20th International Conference on Pattern Recognition, Istanbul, Turkey, 23–26 August 2010; IEEE: Piscataway, NJ, USA, 2010; pp. 2366–2369.
61. Wang, Z.; Simoncelli, E.; Bovik, A. Multiscale structural similarity for image quality assessment. In Proceedings of the Thrity-Seventh Asilomar Conference on Signals, Systems and Computers, Pacific Grove, CA, USA, 9–12 November 2003; IEEE: Piscataway, NJ, USA, 2003; Volume 2, pp. 1398–1402.
62. Xue, W.; Zhang, L.; Mou, X.; Bovik, A.C. Gradient Magnitude Similarity Deviation: A Highly Efficient Perceptual Image Quality Index. *IEEE Trans. Image Process.* **2014**, *23*, 684–695. [CrossRef] [PubMed]
63. Liu, Y.; Xu, X.; Xu, G. MIMO radar calibration and imagery for near-field scattering diagnosis. *IEEE Trans. Aerosp. Electron. Syst.* **2017**, *54*, 442–452. [CrossRef]
64. Bryant, C.; Patton, L.; Rigling, B.; Himed, B. Calibration of Distributed MIMO Radar Systems. *IEEE Trans. Radar Syst.* **2024**. [CrossRef]
65. Manzoni, M.; Tagliaferri, D.; Rizzi, M.; Tebaldini, S.; Guarnieri, A.V.M.; Prati, C.M.; Nicoli, M.; Russo, I.; Duque, S.; Mazzucco, C.; et al. Motion estimation and compensation in automotive MIMO SAR. *IEEE Trans. Intell. Transp. Syst.* **2022**, *24*, 1756–1772. [CrossRef]
66. Ma, X.; Zhang, X.; Ren, Y.; Zhan, X.; Shi, J.; Wei, S.; Zeng, T. Tomographic Imaging with Enhanced Spatial Structures Via a Physics-Aware 3D Reconstruction Network. In Proceedings of the IGARSS 2023—2023 IEEE International Geoscience and Remote Sensing Symposium, Pasadena, CA, USA, 16–21 July 2023; IEEE: Piscataway, NJ, USA, 2023; pp. 1922–1925.
67. Wang, Y.; Zhang, X.; Xu, Y.; Wei, S.; Shi, J. A Covariance Matrix Completion Imaging Method with Coprime Array for MMWAVE Automotive Radar. In Proceedings of the IGARSS 2024—2024 IEEE International Geoscience and Remote Sensing Symposium, Athens, Greece, 7–12 July 2024; IEEE: Piscataway, NJ, USA, 2024; pp. 11206–11209.
68. Sun, S.; Petropulu, A.P. A sparse linear array approach in automotive radars using matrix completion. In Proceedings of the ICASSP 2020—2020 IEEE International Conference on Acoustics, Speech and Signal Processing (ICASSP), Barcelona, Spain, 4–8 May 2020; IEEE: Piscataway, NJ, USA, 2020; pp. 8614–8618.
69. Sun, S.; Zhang, Y.D. 4D automotive radar sensing for autonomous vehicles: A sparsity-oriented approach. *IEEE J. Sel. Top. Signal Process.* **2021**, *15*, 879–891. [CrossRef]

70. Sun, S.; Hu, Y.; Mishra, K.V.; Petropulu, A.P. Widely separated MIMO radar using matrix completion. *IEEE Trans. Radar Syst.* **2024**, *2*, 180–196. [CrossRef]
71. Zhou, L.; Deng, M.; He, J.; Wang, B.; Zhang, S.; Liu, X.; Wei, S. A HRWS SAR Motion Compensation Method with Multichannel Phase Correction. *Remote Sens.* **2024**, *16*, 3544. [CrossRef]

Disclaimer/Publisher's Note: The statements, opinions and data contained in all publications are solely those of the individual author(s) and contributor(s) and not of MDPI and/or the editor(s). MDPI and/or the editor(s) disclaim responsibility for any injury to people or property resulting from any ideas, methods, instructions or products referred to in the content.